



Deposited via The University of Leeds.

White Rose Research Online URL for this paper:

<https://eprints.whiterose.ac.uk/id/eprint/176110/>

Version: Accepted Version

Article:

Shmela, AK, Paton, DA, Collier, RE et al. (2021) Normal fault growth in continental rifting: Insights from changes in displacement and length fault populations due to increasing extension in the Central Kenya Rift. *Tectonophysics*, 814. 228964. ISSN: 0040-1951

<https://doi.org/10.1016/j.tecto.2021.228964>

Crown Copyright © 2021 Published by Elsevier B.V. All rights reserved. This manuscript version is made available under the CC-BY-NC-ND 4.0 license
<http://creativecommons.org/licenses/by-nc-nd/4.0/>.

Reuse

This article is distributed under the terms of the Creative Commons Attribution-NonCommercial-NoDerivs (CC BY-NC-ND) licence. This licence only allows you to download this work and share it with others as long as you credit the authors, but you can't change the article in any way or use it commercially. More information and the full terms of the licence here: <https://creativecommons.org/licenses/>

Takedown

If you consider content in White Rose Research Online to be in breach of UK law, please notify us by emailing eprints@whiterose.ac.uk including the URL of the record and the reason for the withdrawal request.

1 **Normal fault growth in continental rifting: insights from changes in displacement and**
2 **length fault populations due to increasing extension in the central Kenya Rift**

3
4 Ahmad K. Shmela ^{a, *}, Douglas A. Paton ^b, Richard E Collier ^c, Rebecca E. Bell ^d

5 ^{a, c} University of Leeds, School of Earth and Environment

6 ^bTectonKnow Ltd., Settle, North Yorkshire

7 ^d Imperial College London, Department of Earth Science & Engineering

8
9
10 **Keywords:** Scaling properties, Strain accommodation, Fault growth, Rift evolution

11 **Highlights**

- 12 • Examination of upper crust brittle deformation during continental rifting from DEM data.
13 • Examination of fractal dimension of power law fit of fault populations with increasing strain.
14 • Determination of fault growth models from fault population scaling properties.

15 **Abstract**

16 This study examines the scaling relationship between fault length and displacement for the purpose of gaining
17 a better understanding of the evolution of normal faults within the central Kenya Rift. 620 normal faults were
18 manually mapped from a digital elevation model (DEM), with 30 m² resolution and an estimated maximum
19 displacement of ~40 – ~6030 m and fault lengths of 1270 - 60600 m. To assess the contribution of fault
20 populations to the strain accommodation from south to north, the study area has been divided into three zones
21 of fault populations based upon their average fault orientations; zone 1 in the north is dominated by NNE
22 striking faults, zone 2 in the centre of the rift is characterised by NNW to NNE fault trends, whereas zone 3
23 in the south is characterised by NNW striking fault systems. Extensional strain was estimated by summing
24 fault heaves across six transects along the rift, which showed a progressive increase of strain from south to
25 north. The fault length and displacement data in the three zones fit to a power law distribution. The cumulative
26 distributions of fault length populations showed similar fractal dimension (D) in the three zones. The
27 cumulative displacement distributions for the three zones showed a decrease in the Power-law fractal
28 dimension with increasing strain, which implies that the strain is increasingly localised onto larger faults as
29 the fault system becomes more evolved from south to north. Increasing displacement with increasing strain
30 while the fault length remains almost constant may indicate that the fault system could be evolving in
31 accordance with a constant length fault growth model, where faults lengthen quickly and then accrue
32 displacement. Results of this study suggest that the process of progressively increasing fault system maturity

33 and strain localization onto large faults can be observed even over a relatively small area (240 x 150 km)
 34 within the rift system. It is also suggested that patterns of fault growth can be deduced from the fractal
 35 dimension of cumulative distribution of fault size populations.

36 **1 Introduction**

37 Observations of fault size, specifically displacement versus length distributions can be used to help understand
 38 rift development (e.g. Gupta and Scholz, 2000). Moreover, in order to understand the surface deformation of
 39 tectonically active regions, it is critical to understand the evolution of normal faulting associated with rifting
 40 and extensional processes.

41 Quantitative analyses of fault population parameters, such as trace-length, and displacement as well as
 42 displacement distributions have been studied in recent decades in many studies (e.g. Cowie and Scholz, 1992a,
 43 Dawers et al., 1993, Schultz and Fossen, 2002, Walsh et al., 2002b, Soliva and Schultz, 2008, Torabi and
 44 Berg, 2011, Torabi et al., 2019) in order to understand the growth history of fault populations. Such analyses
 45 have also been used to suggest a number of fault growth models including fault growth by radial propagation
 46 (Walsh and Watterson, 1988), a coherent fault model of segment linkage of fault arrays by Cartwright et al.
 47 (1995) and an alternative fault growth model suggested by e.g. Walsh et al. (2002a) and Rotevatn et al. (2019),
 48 where fault lengths are near constant from an early stage and growth is largely achieved by an increase in
 49 fault displacement.

50 Cumulative frequency distribution functions (CDF) are the most common way to describe attributes of fault
 51 populations (e.g. length, displacement) and have been used in many studies (e.g. Walsh et al., 1991, Jackson
 52 and Sanderson, 1992, Cladouhos and Marrett, 1996, Bonnet et al., 2001). Most populations of fault lengths
 53 and displacements have been found to plot along a more or less straight line in log-log space (e.g. fault length
 54 vs. cumulative number) which implies a power-law distribution (e.g. Watterson et al., 1996, Ackermann and
 55 Schlische, 1997, Poulimenos, 2000, Gillespie et al., 2001, Peacock, 2002, Bailey et al., 2005, Soliva and
 56 Schultz, 2008, Torabi et al., 2019). This power-law distribution is described mathematically as:

$$57 \quad N = aS^{-D}$$

58 where S is fault offset (i.e. length, displacement, throw or heave), N is the cumulative number of fault offset,
 59 and a is a constant. D is an exponent, and it describes the fractal dimension of slope of the straight segment
 60 (Walsh et al., 1991, Yielding et al., 1996)

61 It has been demonstrated in several studies that differences in the value of the exponent D (the fractal
 62 dimension) are attributed to variations in the amount of strain accommodated by fault systems, and it may
 63 also change for different stages of fault evolution (i.e. fault nucleation, propagation and amalgamation) (e.g.
 64 (e.g. Cowie et al., 1995, Cowie, 1998a, Ackermann et al., 2001, Bailey et al., 2005). It has also been found

65 that the fractal dimension is inversely related to the strain, where the former decreases systematically as the
66 latter increases and vice versa (e.g. Cartwright et al., 1995, Poulimenos, 2000, Moriya et al., 2005). Therefore,
67 analysis of the fractal dimension of power law distributions can be used to characterize the spatial distribution
68 of faults (Cowie, 1998a, Sornette et al., 1993). It was also found that high fractal dimensions reflect a greater
69 proportion of small faults relative to larger faults than lower fractal dimensions (Marrett and Allmendinger,
70 1991, Yielding et al., 1996)

71 The aims of this paper are to quantitatively investigate fault scaling relations (fault length and displacement)
72 of three different fault populations for the purpose of providing insights into the evolution of normal fault
73 systems in the central Kenya Rift. To achieve this aim, a Digital Elevation Model (DEM) with 30 m horizontal
74 resolution is used to produce a detailed fault geometry dataset for surface faults of the central Kenya Rift. 620
75 faults have been manually mapped from this DEM over an area measuring 240 x 150 km. In this study, we
76 measured the throw and length of surface faults derived from ASTER DEM data. Second, we estimated the
77 part of fault throws obscured due to burial by volcanics and sediments in the hanging wall. Fault throw was
78 then used to calculate the maximum displacement using an average fault dip for the central Kenya rift. The
79 effect of data resolution on the fault trace length was also corrected by adding an estimated tip length. Next,
80 three domains of differing fault populations have been identified, which offer an opportunity to investigate
81 fault scaling relations of the fault populations along the central Kenya Rift during progressive deformation.
82 Finally, we discuss the results addressing implications for the evolution of the rift and the growth of normal
83 faults in the study area.

84

85 **2 Tectonic and geological background**

86 The spatial extent of this study covers a portion of the central Kenya Rift located between Lat 1.05° N to -1°
87 S and Long 35.5° to 36.7° E that covers an area of 240 x 150 km (Figure 1). The central Kenya Rift is thought
88 to represent a phase of relatively early continental rifting (Baker and Wohlenberg, 1971) where most
89 deformation is accommodated on small boundary faults with an absence of internal faults (e.g. Corti, 2009,
90 Agostini et al., 2011b). The northern part of the central Kenya Rift comprises two parallel Rift valleys (Figure
91 2). The eastern rift is known as the Kenya Rift and the western one is called the Kerio Rift, separated by the
92 Kamasia horst, and these structures are oriented N10°E (Figure 2). Both Rift basins are west-dipping half-
93 grabens, with major border faults on the western rift shoulders, the Kerio Rift terminating west of Lake
94 Bogoria, while the Kenya Rift continues farther to the south and bends sharply at the Gregory Rift (Figure 2).
95 This bend has been interpreted as the intersection with a large NW trending basement structure known as the
96 Aswa lineament (Smith and Mosley, 1993, Chorowicz, 2005, Omenda, 2010).

97 The central segment of the Kenya rift system is known as the Gregory Rift (Figure 2) and is a complex graben
98 that trends N-S. It is 60 -70 km in width and is bounded by en echelon arrangements of major normal faults
99 forming the Nguruman, Mau, and Elgeyo escarpments on the western boundary and the Aberdare escarpment
100 on the eastern boundary (Jones and Lippard, 1979, Baker et al., 1988) (Figure 2). Fault escarpments are well
101 defined and reach up to 2000 m in height (Baker and Wohlenberg, 1971). The central Kenya rift encompasses
102 a number of half graben basins that have varying orientations ranging from NNE-SSW to NNW-SSE (Smith
103 and Mosley, 1993). The major faults in the central Kenya Rift are antithetic and dominantly dip eastwards
104 (Baker and Wohlenberg, 1971, Baker et al., 1972). Overall, the tectonostratigraphic evolution of these Rift
105 sectors shows a successive migration of normal faulting from the boundary faults inwards toward the Rift
106 valley , where the structural development has been characterized by a concentration of faulting associated
107 with volcanism since late Pliocene era (Baker and Wohlenberg, 1971).

108 Volcanism and rifting started in the Kenya Rift around the early Miocene in the north, in the Lake Turkana
109 area and migrated southwards. Rifting was active from around the middle to late Miocene in the central
110 segment (Baker et al., 1972, Smith and Mosley, 1993). The Kerio basin in the centre and the Baringo basin
111 in the north of the central Kenya Rift witnessed a long period of extensive basaltic lava extrusion during the
112 initial phase of rifting (Paleogene to lower Miocene) (Ebinger, 1989). Therefore, infill in the central Kenya
113 Rift is predominantly volcanogenic (Smith, 1994). Furthermore, a geological map of Kenya (Ministry of
114 energy of Kenya 1987, Figure 1) shows that the study area is covered by Quaternary and Tertiary volcanic
115 sediments. The thickness of sediments and volcanic deposits in this region is ~4.5-5km (Hautot et al., 2000)
116 as determined from magnetotelluric (MT) data, which is a geophysical method used to model the Earth's
117 subsurface from measurements of natural geomagnetic and geoelectric field variation at the Earth's surface.

118 It has been proposed that faults in the East African Rift System (EARS) are not randomly distributed but tend
119 to follow the trend of pre-existing weakness zones within the lithosphere i.e. Proterozoic mobile belts, and
120 avoid the Archaean stable cratonic areas (McConnell, 1972, Daly et al., 1989, Petit and Ebinger, 2000, Ziegler
121 and Cloetingh, 2004). The central Kenya Rift segments formed along old zones of weakness at the contact
122 between two contrasting types of lithosphere; the Archean Tanzanian craton and the Proterozoic Mozambique
123 belt (e.g. Smith and Mosley, 1993, Mariita and Keller, 2007). Therefore, the extensional deformation may be
124 localized along mobile belts and suture zones as they tend to be weaker than the surrounding areas (Petit and
125 Ebinger, 2000).

126

127

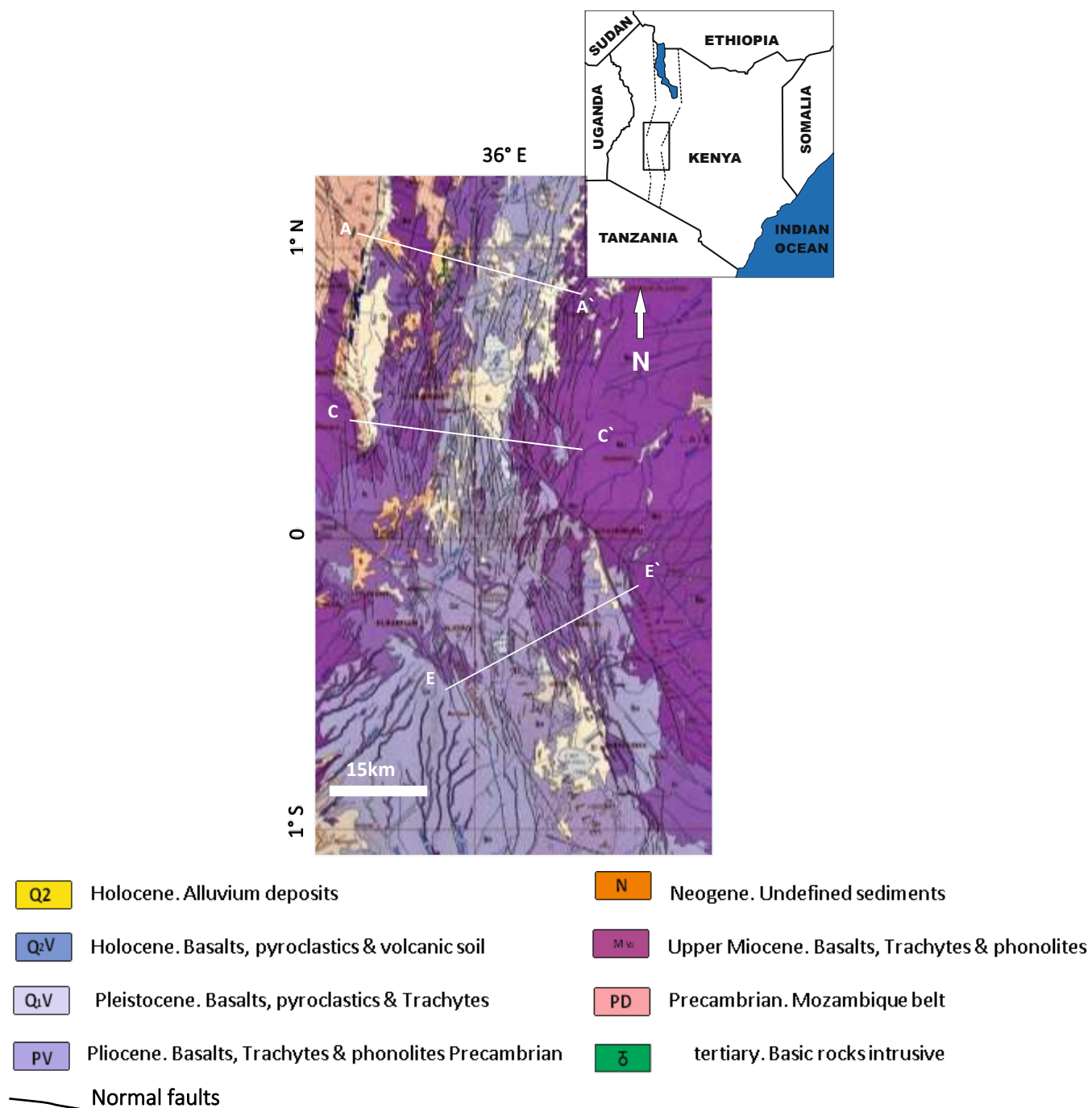


Figure 1. a geological map of the study area, from geological map of Kenya (Ministry of Energy of Kenya 1987). The small inset image displays the location of the study area, the central Kenya rift. The white lines are locations of the topographic profile shown in figure 8.

128 **3 Methodology**

129 **3.1 Data and interpretation of fault traces**

130 In this study, 620 discrete faults were identified, from which fault measurements were made such as fault
131 trace length, maximum apparent throw, orientation, and throw/length ratio. Maximum apparent displacement
132 was derived from each maximum fault throw value using an average fault dip of 65° . There are several reasons
133 for using an average fault dip in this regional study: firstly, fault dips cannot be directly measured from
134 ASTER DEM data. Secondly, lack of fault dip data in previous studies for the study area and thirdly, the large
135 number of faults involved in this study that required a generalized assumption. This fault dip value of 65° is
136 the average of a fault dip range of 55° to 75° for the central Kenya Rift as reported in Zielke and Strecker
137 (2009).

138 Digital elevation models (DEM) are the main data used to investigate the upper crust brittle deformation in
139 the study area. The DEM data were obtained from the USGS (<https://lpdaac.usgs.gov/>) through Advanced
140 Space-borne Thermal Emission and Reflection Radiometer (ASTER) data with ground resolution of 30 m x
141 30 m and vertical resolution of 20 m to provide information on the morphology of surface faults. Google
142 Earth optical spectrum imagery with a resolution of about 15 m was used along with the ASTER DEM to
143 assist in viewing the topography and determine the dip direction of the mapped faults. The data resolution
144 refers to the minimum distance by which data can be recorded from the scanned scene. The main effect of
145 resolution is a truncation, which means fault trace lengths below 30 m (found in fault tips) and fault heights
146 (throws) below 20 m cut-offs are not resolvable, which lead to underestimation of these parameters. However,
147 the effect of truncation is more significant on small size fault populations (Walsh et al., 1996, Watterson et
148 al., 1996, Yielding et al., 1996)

149 The DEM data were converted into a shaded relief surface (Figure 2). Fault traces were identified on the DEM
150 surface by using several techniques available in Petrel software, including edge detection, which is
151 particularly useful in identifying where subtle changes in the surface topography occur, thereby enhancing
152 confidence in mapping fault escarpments. Vertical exaggeration of x5 was also used to facilitate tracing fault
153 scarps. Given the resolution of the DEM used, some topographic features (i.e. <20 m height) that do not show
154 clear topographic scarps were not considered to be faults. Nevertheless, hundreds of fault scarps were readily
155 distinguishable on the DEM surface across the study area. Fault scarps were interpreted and recorded based
156 on their length, and when fault segments were linked, the entire length of the fault segment array was mapped
157 as a single larger fault.

158 In this study, the height of fault scarp measured from the DEM has been used as a proxy for fault throw.
159 However, accumulation of sediment, volcanic and erosional deposits reduce the apparent height of the fault

160 scarp. Moreover, fault blocks are normally eroded, and in DEM surfaces, it is not possible to determine how
161 much erosion of the block has occurred. All these uncertainties may introduce systematic error into throw
162 measurements and strain estimations. For each fault, footwall cut-offs were manually digitized by tracing the
163 crest of each topographic scarp along strike (blue dots on blue lines in Figure 3A –C), whilst apparent hanging
164 wall cut-offs were picked by tracing the lower-most position of the fault along its trace (pink dots on pink
165 lines in Figure 3A – C). Therefore, the measured throw was the maximum value of the apparent fault height/
166 throw between the corresponding points picked in the footwall cut-off and the hanging wall cut-off along each
167 fault trace measured in two dimensions (2D). Fault length defined in this study is the horizontal exposed fault
168 trace length along strike.

169 The chronology of fault formation in the central Kenya rift is that major faults were first formed between 16
170 and 8 Ma (Smith, 1994), and the volcano-sedimentary infill in the rift is between 4.5-5km thick (Hautot et al.
171 (2000). Consequently, fault throws, and lengths measured at this stage are just the apparent or exposed values
172 of fault throw, and length due to possibility of hanging walls being partially filled with sediment, volcanic
173 and erosional deposits, and subsequent burial of fault tips.

174

175

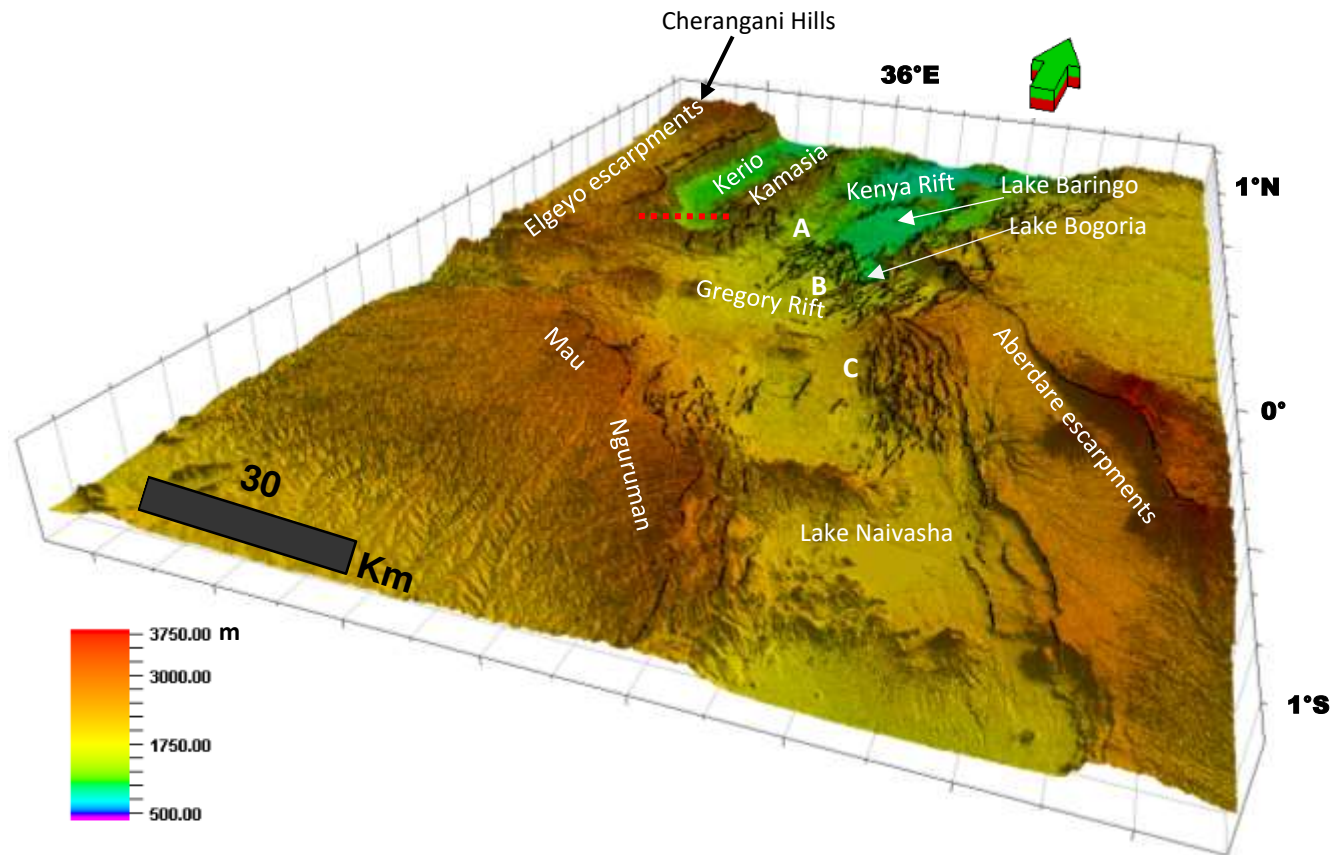


Figure 2. A shaded relief surface image generated from ASTER DEM. The small inset image displays location of study area within the East Africa Rift System; dashed red line is a location of seismic line shown in (Figure 4); A, B and C are locations of close-up images (Figure 3)

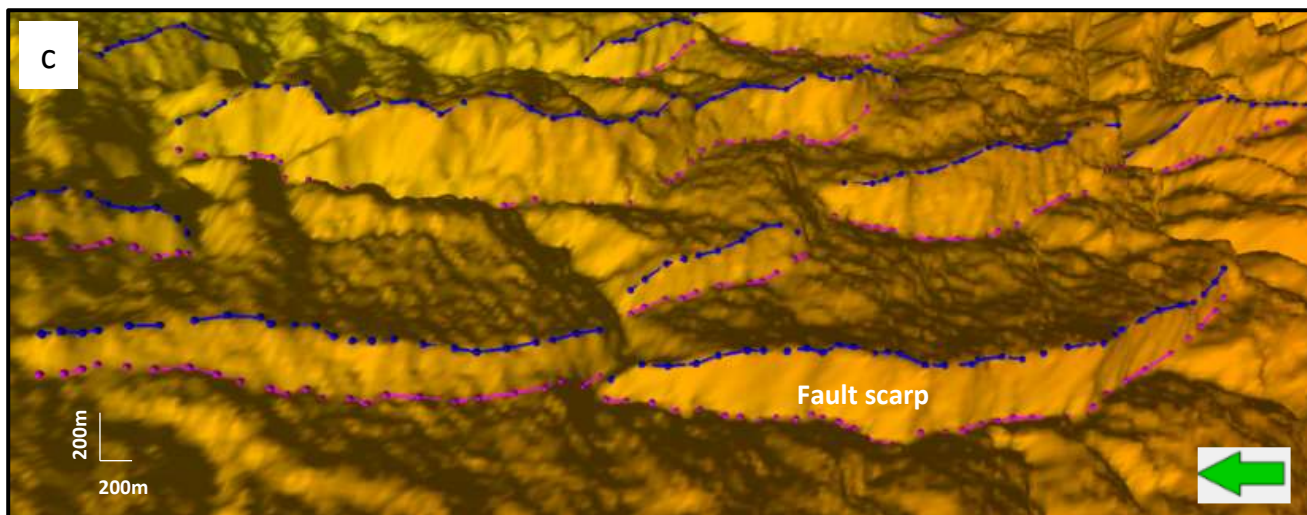
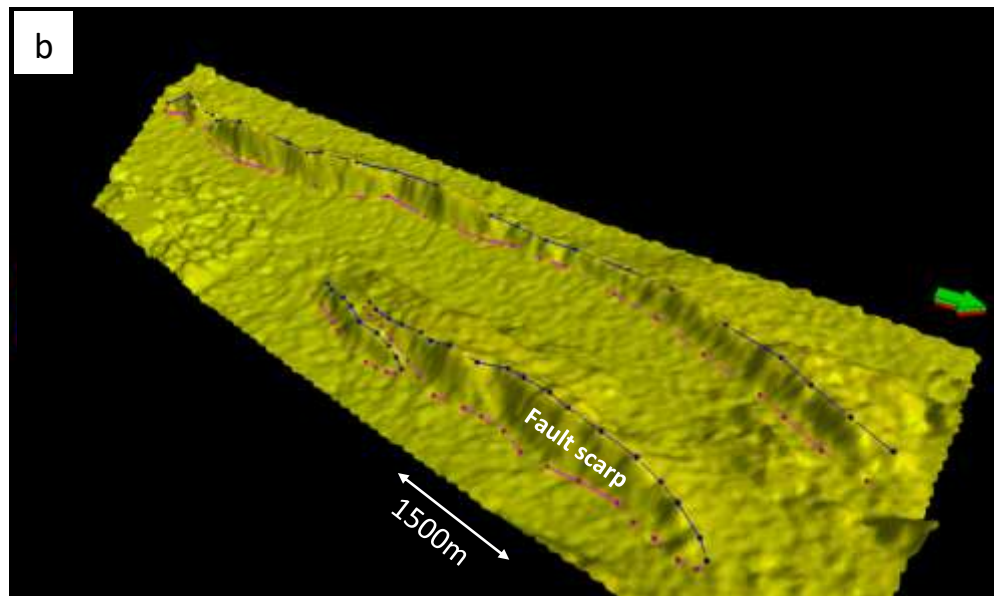
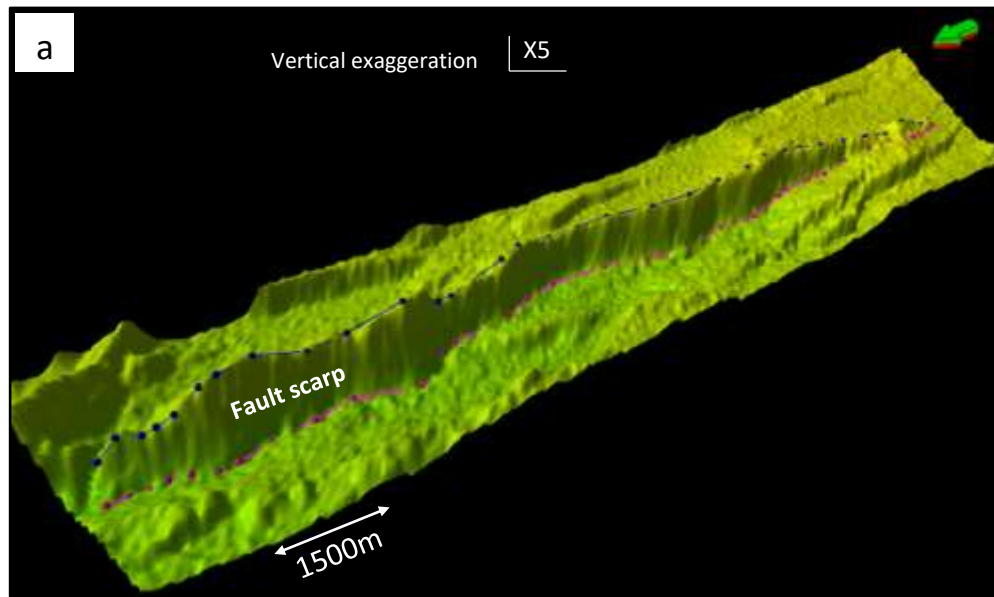


Figure 3. Examples to show how the faults were picked using the DEM surface. The footwall cut-off is picked (shown as blue circles on blue polyline) followed by picking the corresponding apparent hanging wall cut-off (pink circles on pink polyline), resulting in the same number of picks top and bottom, which were used to calculate throw. a) Fault scarp structure shows the final picks for the footwall and hanging wall cut-offs. b) Fault structure on the left-hand side of the image is an example of fault picking along two faults separated by a relay ramp. c) Picks along several en echelon fault scarps in the central part of the study area. (See Figure 2 for image locations).

177

178 **3.2 Under sampling of faults lengths due to truncation bias.**

179 Data resolution and burial of fault tips may mask the true positions of fault tips at the surface and therefore
 180 cause fault lengths to be underestimated. Truncation bias refers to effects caused by systematic under-
 181 representation of smaller faults in a sample due to limitations in data resolution, below which the fault length
 182 and throw cannot be detected (Pickering et al., 1995, Watterson et al., 1996, Zhang and Einstein, 2000, Bonnet
 183 et al., 2001). This truncation bias needs to be corrected for, to provide a more reliable estimate of the fault
 184 trace length. However the effects of truncation are relatively more significant on small scale fault populations
 185 (Walsh et al., 1996, Watterson et al., 1996, Yielding et al., 1996). Censoring bias refers to partial sampling of
 186 large faults that extend beyond the sample area and therefore are incompletely characterized (Pickering et al.,
 187 1995, Zhang and Einstein, 2000, Bonnet et al., 2001). Censoring is thought to not be of great significance
 188 unless the sample area is small relative to the full lengths of the majority of fault traces (Heffer and Bevan,
 189 1990).

190 It has been shown in some studies such as Pickering et al. (1997) and Soliva and Schultz (2008) that the
 191 truncation bias can be estimated by dividing the lowest throw value that can be resolved by the average value
 192 of throw/length ratio in a given region. The average throw/length ratio calculated for this study area was 0.04,
 193 which is similar to that estimated by Le Gall et al. (2008), in southern Kenya close to the Tanzania border.
 194 Given the vertical resolution of 20m ASTER DEM (<https://lpdaac.usgs.gov/>), we estimate that a truncation
 195 bias occurs for fault lengths less than 500 m. To account for the truncation bias, we added a 500 m to the end
 196 of each fault to enable us to estimate the true distribution of fault lengths. By adding the 500 m to fault tips
 197 of the 620 mapped faults, the length populations range from 1270 m to 60600 m, with an average length of
 198 6150 m.

199

200 **3.3 Under sampling of fault throws and derivation of displacements**

201 In this study we quantified throw as the height of the fault scarp measured from the DEM. The extent of total
202 fault throws into the subsurface is hard to be constrained due to the scarcity of seismic data over this region
203 of the EARS. However, a seismic line (Figure 4b) shown in Morley and Ngenoh (1999c) was used in an
204 attempt to account for the missing throw. This seismic line was shot by the National Oil Corporation of Kenya
205 (NOCK) in 1990 over at the southern end of the Kerio Rift between the Elgeyo escarpment and the Kamasia
206 horst (see Figure 2 for location). According to the interpretation by Pope (1992) and Ngenoh (1993), this
207 seismic line shows a large boundary fault, namely the Elgeyo Fault in the subsurface, which marks the western
208 boundary of the Rift (Figure 4b). The DEM image resolves the continuation of the Elgeyo escarpment at the
209 surface (Figure 4a).

210 From the seismic line (Figure 4 b) we interpret the Elgeyo Fault hanging wall cut-off to be at a depth of ~ 2
211 sec (TWT) (Figure 4c). Given that the average seismic velocity for the rift infill between Lake Baringo and
212 Lake Naivasha is about 4000 m/s as determined by Henry et al. (1990b), the subsurface fault throw is therefore
213 about 4 km. This value is in general agreement with the thickness of volcanic-sedimentary infill of ~ 4.5 km
214 estimated in Hautot et al. (2000) using Magnetotellurics (MT), and an estimate of 4km in Henry et al. (1990b)
215 that derived the thickness of the sediment/volcanics layer from two seismic refraction lines in the central
216 Kenya Rift. Consequently, the buried throw is about 2.5 times the apparent throw of ~ 1560 m estimated from
217 the surface scarp of the Elgeyo escarpment. Since there have been no detailed regional studies that recorded the
218 volcano-sedimentary infill in different parts of the central Kenya rift, and also due to the lack of adequate
219 subsurface data in this rift, the buried throw of different size faults across the rift cannot be established. Therefore,
220 for simplicity, we assumed that all mapped faults extend under the surface by the same factor of 2.5 time as
221 that calculated for the Egeleyo escarpment. So, the correction consists of simply multiplying each surface
222 apparent fault throw measurement by 2.5 and adding the apparent surface throw for each mapped fault.
223 Consequently, the estimated maximum throw range is ~ 37 to ~ 5460 m with an average of ~ 450 m. Fault
224 displacements were then derived from fault throws through a simple geometric calculation using a
225 representative fault dip of 65° .

226

227

228

229

230

231

232

233

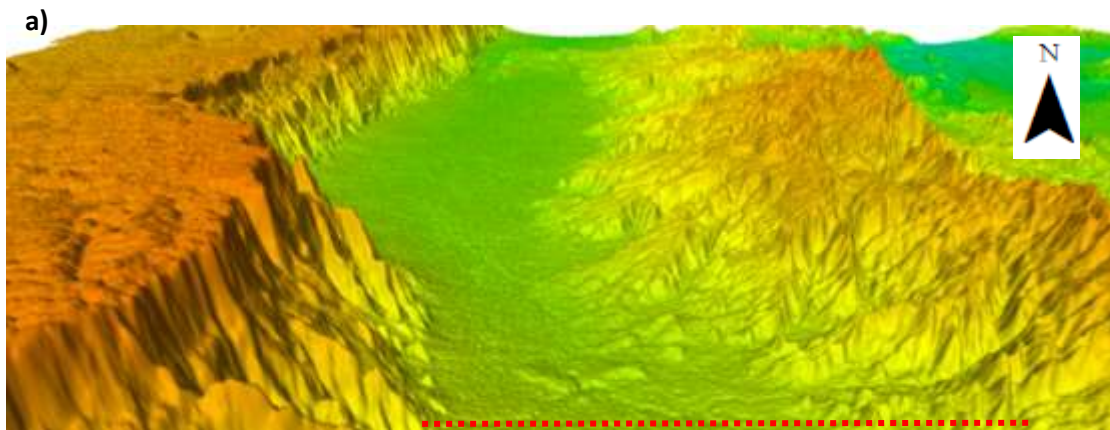
234

235

236

237

238



239

240

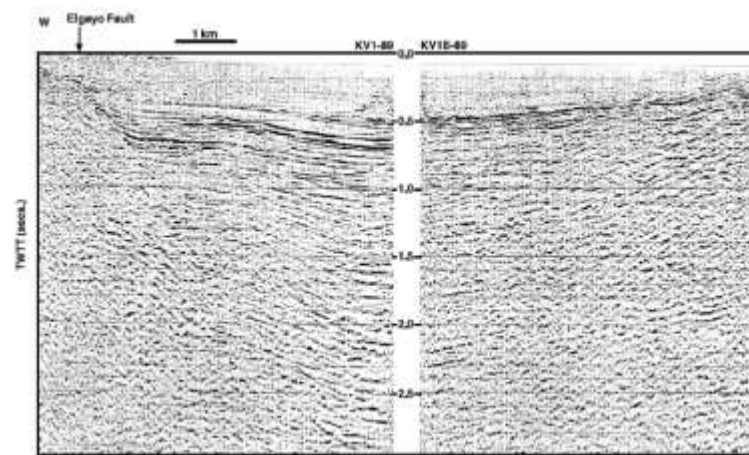
241

242

243

244

b)



c)

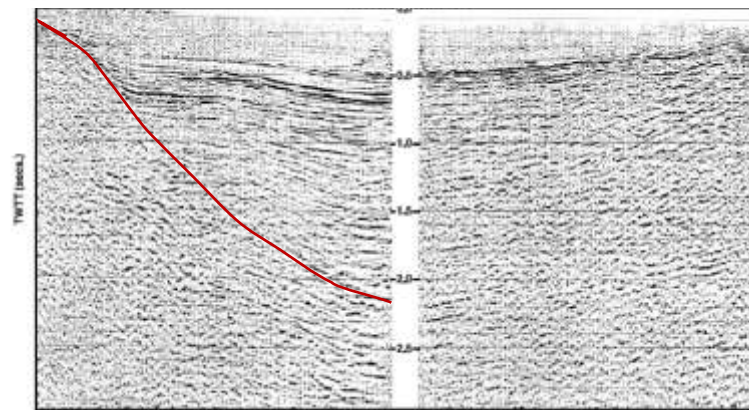


Figure 4. a) DEM surface showing the Elgayo Fault escarpment, dashed red line shows the location of seismic line, which is about 12 km in length (see Figure 1). b) seismic line in the Kerio Rift from Morley and Ngenoh (1999c). c) interpretation of the Elgayo Fault.

245 3.4 Fault analysis methods

246 As part of examining the 620 faults mapped from the DEM surface, the relationship between fault
 247 displacement and fault length is plotted and compared with a global data set of normal faults. It has been
 248 largely accepted that the relationship between displacement and fault length provides crucial information on
 249 the growth of faults through time (e.g. Walsh and Watterson, 1988, Cowie and Scholz, 1992b). The
 250 relationship between the maximum displacement (D) and the fault length (L) has been defined as follows (e.g.
 251 Walsh and Watterson, 1988, Dawers et al., 1993):

$$252 \quad d_{max} = cL^n$$

253 where c is a constant relating to material properties, n is the exponent value, which ranges from 0.5 to 2.0 for
 254 tectonic fault systems. published values of n are; $n = 0.5$ (Fossen and Hesthammer, 1997), $n = 1.0$ (Cowie and
 255 Scholz, 1992a, Dawers et al., 1993, Schlische et al., 1996, Davis et al., 2005, Stanton-Yonge et al., 2020), n
 256 $= 1.5$ (Marrett and Allmendinger, 1991, Gillespie et al., 1992) and $n = 2.0$ (Watterson, 1986, Walsh and
 257 Watterson, 1988), The n value of fault Displacement/Length data has implications for what fault model best
 258 describes the growth of faults.

259 In this paper, the trend of extensional strain from south to north of the study area was estimated by measuring
 260 total fault heave across faults along six transects along the rifts (Figure 3), in order to determine the
 261 contribution of different fault populations to the strain. The horizontal fault separation (heave) was estimated
 262 by measuring the horizontal distance between the hanging-wall and footwall cut-offs, measured perpendicular
 263 to the trace of the fault in map view (2D) for all faults that intersect the cross-sections. However, volcanic and
 264 sediment infill as well as eroded faults scarps prevent identifying the original positions of faults hanging wall
 265 and footwall cut-offs, which in turn would introduce some uncertainties on heave measurements. Moreover,
 266 the extensional strain may also be underestimated due to underrepresentation of small faults that fall below
 267 the resolution of observation.

268 Fault displacements and fault lengths were analysed through fault cumulative frequency plots. This can be
 269 done through ranking the displacement/length data in a descending order and then plotting fault
 270 displacement/length data against the cumulative frequency in a log-log scale. Different statistical functions
 271 (i.e. power law, lognormal and exponential laws) have been used to examine the best fit for the fault
 272 displacement/length data. These statistical functions deploy a transformed regression model, which is a type
 273 of least squares estimation method to fit statistical distributions that has been widely used in geological studies
 274 (Pickering et al., 1995, Poulimenos, 2000, Peacock, 2002, Bailey et al., 2005, Soliva et al., 2006, Soliva and
 275 Schultz, 2008).

276

277 **4 Fault Population analysis and results**

278 **4.1 Relationship between fault length and displacement**

279 Fault displacement and length data obtained in this study were compared with previously published
280 displacement-length data (Figure 5) for normal faults from different sources compiled by Gillespie et al.
281 (1992) and Bailey et al. (2005). The mapped faults lie well within the published global dataset.

282 Fault maximum displacement and length data from the three zones were plotted in different colors in a log-
283 log space (Figure 6a). The data from the three zones combined showed a large scatter that spans about two
284 orders of magnitude in both variables. A linear regression line passing through the data points is expressed as
285 $y = 0.0691x^{+129.5}$ with coefficient of determination $R^2 = 0.479$ and a power law fit, with a slope of $n = 1.09$
286 and $R^2 = 0.382$. The low coefficient of determination together with the large extent of scatter cannot justify
287 the regression lines. The maximum displacement-length data for each individual zone also exhibited a low
288 coefficient of determination for both linear and power law trendlines due to the high scatter. Such scatter is
289 common to other fault population studies and has been attributed to: combining data sets from areas of
290 different lithology and material properties (e.g. Cartwright et al., 1995, Peacock and Sanderson, 1991,
291 Peacock, 2002, Cowie and Scholz, 1992a), fault growth and segment linkage (Cartwright et al., 1995,
292 Schlische et al., 1996, Cartwright et al., 1996, Mansfield and Cartwright, 2001), sampling effects and
293 inaccurate measurement (Gillespie et al., 1992). However, despite this high scatter, it can be observed from
294 displacement-length data for each individual zone (Figure 6b, c, d), where several faults have a comparable
295 length but varying displacement, that this will lead to increasing displacement-length ratios for larger faults,
296 and create a general vertical trend of increasing displacement for those faults which have fixed length but
297 accumulate throw.

298

299

300

301

302

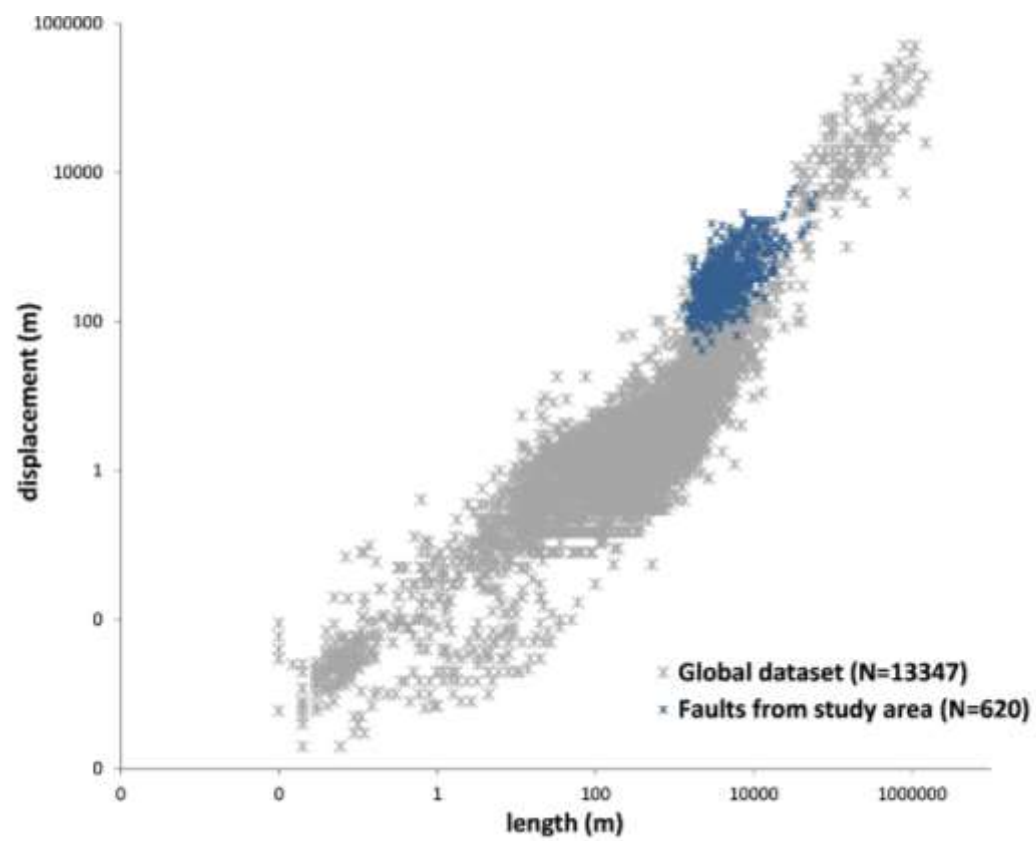


Figure 5. Log-log plot of fault displacement vs. length for faults from the study area along with previously published data from (Gillespie et al., 1992, Bailey et al., 2005).

303

304

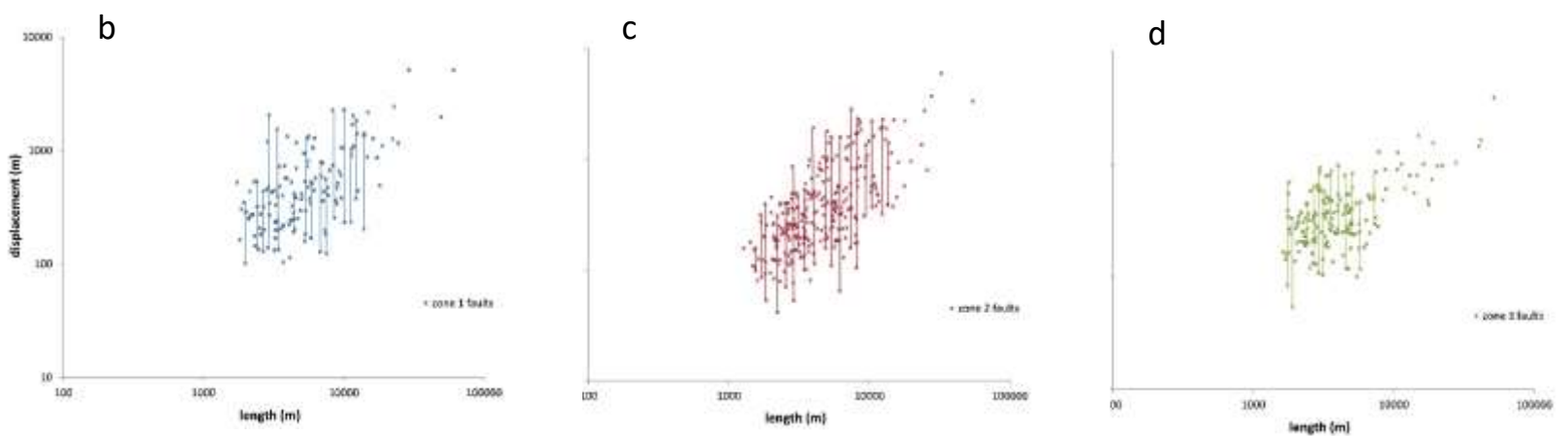
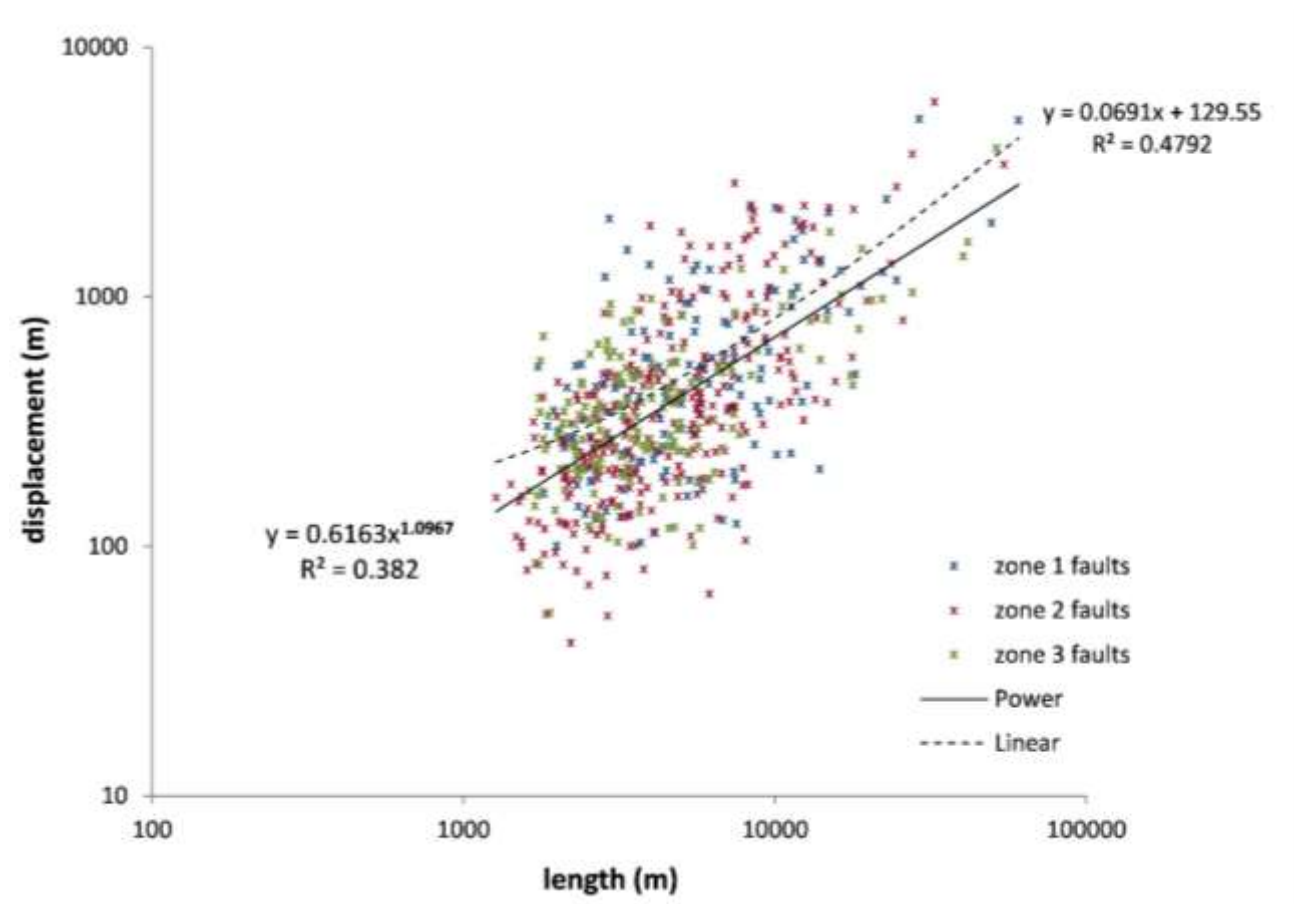


Figure 6. (a) Log-log plot for displacement vs length for all faults mapped in the study area showing a large scatter. (b, c & d) Displacement vs. length plots of individual fault zones, faults showing comparable length, but varying displacement are joined by lines to illustrate the observed vertical trend of increasing displacement population..

305 **4.2 Relationships between strain and fault populations**

306 There are different fault orientations throughout the study area (Figure 7). Therefore, to assess the
 307 contributions of different fault sets to the strain accommodation of the entire area, the region was divided into
 308 three subzones (zone 1, zone 2 & zone 3) based upon average fault orientations (Figure 7). Zone 1, in the
 309 north is dominated by N-NNE striking faults, zone 2 in the central section of the rift is characterised by a
 310 NNW to NNE fault strike, whereas zone 3 in the south is characterised by a N-NNW striking fault system
 311 (Figure 7). The number of resolved faults is 149, 295 and 177 for zone 1, zone 2 and zone 3 respectively.

312 Normal faults typically form perpendicular to the stress direction. The average fault orientation for zone 3
 313 (shown as a red line in the rose diagrams in Figure 7) is $\sim 10^\circ$ oblique from being perpendicular to the regional
 314 EW-trending extension orientation, and more oblique compared to zone 2 and zone 1. In theory, such obliquity
 315 would cause the displacement vector to deviate from true dip-slip and produce what is called an oblique-slip
 316 fault. However, the true displacement vector cannot be estimated from a DEM in such a regional study,
 317 because defining a fault as oblique requires both dip and strike components to be measurable and significant.
 318 Therefore, for the purpose of this study, we assumed the effect of $\sim 10^\circ$ obliquity between the average fault
 319 orientation and the EW-trending regional extension in zone 3 to be insignificant, and consequently error
 320 associated with calculating displacement from the apparent throw measurements to be also negligible.

321 **4.3 Strain accommodation**

322 Fault heaves are an expression of strain in extensional tectonic settings. Fault displacement (i.e. heave and
 323 throw) increases as strain accumulates (e.g. Poulimenos, 2000, Walsh et al., 2002a, Schlagenhauf et al., 2008).
 324 Therefore, in this study, we consider that total (cumulative) heave and associated heave percentage (Table 1)
 325 are illustrative of strain. The strain along the rift from south to north was then assessed using six cross-sections
 326 (Figure 7). The cross-sections were defined perpendicular to the trend of fault populations in each zone. We
 327 present two cross-sections for each zone, AA' & BB' in zone 1, CC' & DD' in zone 2 trend ESE-WNW and
 328 EE' & FF' in zone 3 trend ENE-WSW (Figure 7). Total fault heave that has been taken as representative of
 329 strain was then estimated by summing fault heaves across each cross-section. This analysis shows that average
 330 strain in each zone increases from ~ 5560 m in zone 3 (south) to ~ 7470 m in the central (zone 2), whereas
 331 zone 1 in the north exhibited the largest average extension of ~ 9800 m (Table 1). The percentage of strain
 332 accommodated at each cross-section in relation to the overall strain of the study area was defined by dividing
 333 the amount of strain of each transect by the total amount of strain estimated for the entire study area (Table
 334 1). Figure 9 shows a progressive increase of strain from zone 3 in the south to zone 1 in the north. Estimations
 335 of uncertainty in measurements of each total heave (**Error! Reference source not found.**) did not show a
 336 significant error contribution (Figure 9).

337 (Figure 8) shows topographic profiles of cross-sections AA`, CC` and EE` respectively. These profiles show
338 that the width of the rift valley widens from 19 km in the south (cross-section EE`) to 40 km in the north
339 (cross-section AA`). Elevation of the rift valley also decreases from ~2000 m in the south (cross-section EE`)
340 to ~1000 m in the north (cross-section AA`), where rift valleys of the Kero Rift and the Kenya Rift appear to
341 be in the lowest part of the study area. This systematic decrease in rift floor elevation is interpreted to reflect
342 increased lithospheric thinning and subsidence, as indicated by Cowie et al. (2005). The geological formations
343 shown in the cross-sections depict extensive volcanic deposits along the rift as reported by Ebinger (1989).

344

345

346

347

348

349

350

351

352

353

354

355

356

357

358

359

360

361

362

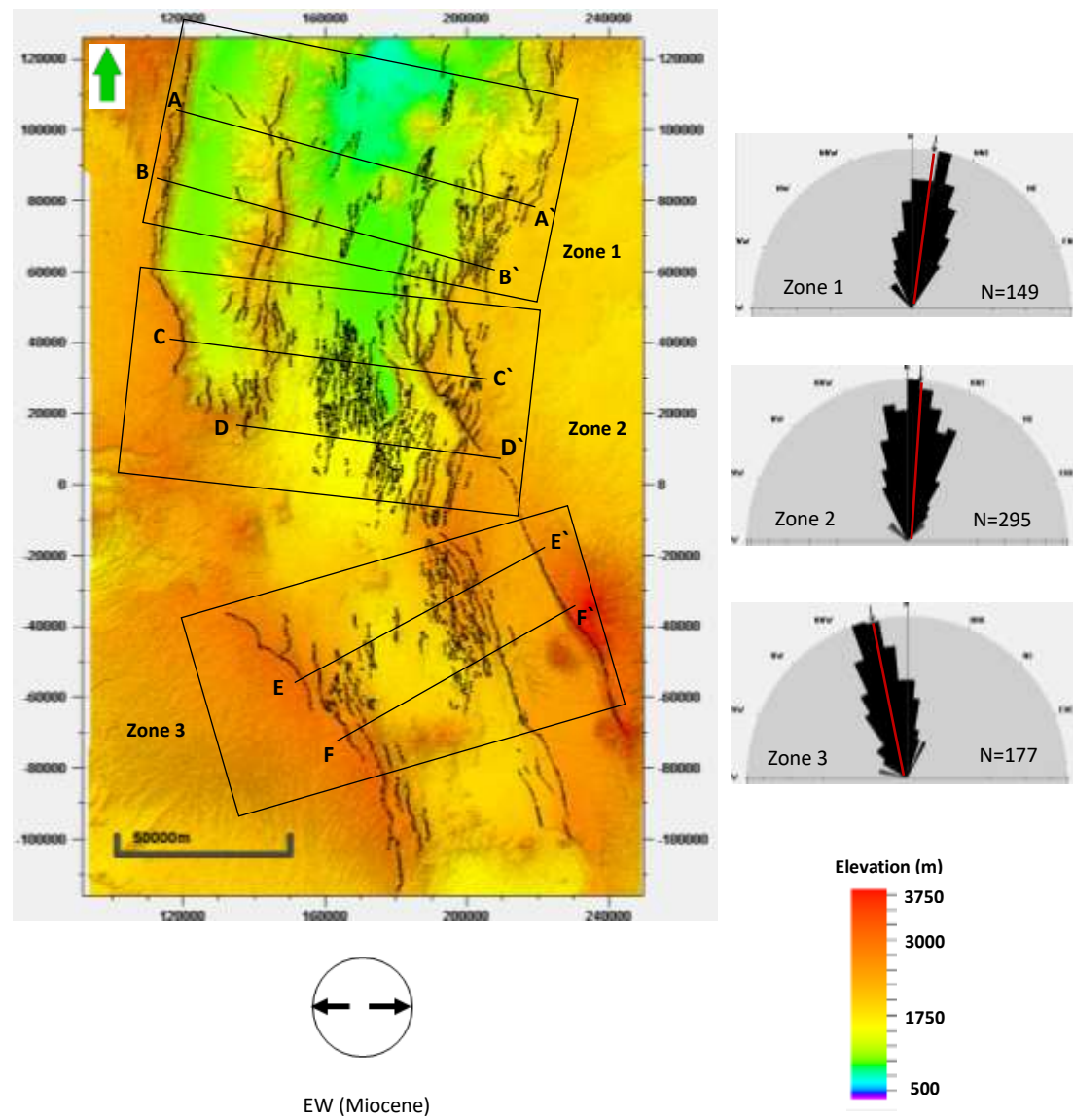
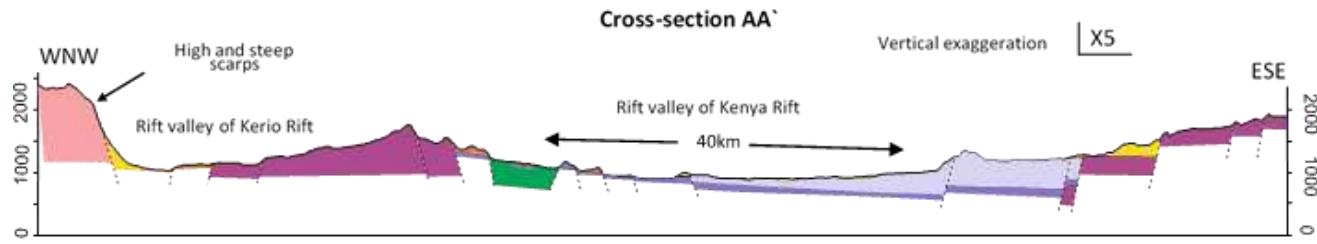


Figure 7 . Rectangles represent the three structural zones defined within the study area, and location of cross-sections (see Figure 2 for location of the 3D surface). The two opposite arrows indicate extension direction, and the red line within the rose diagrams shows the average orientation of fault population.

363



364

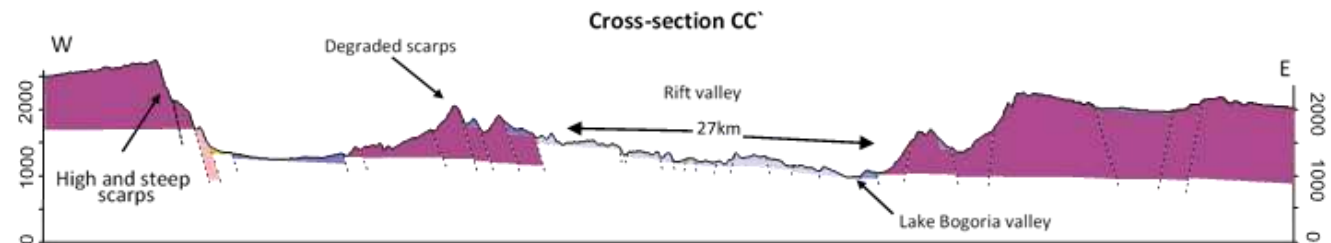
365

366

367

368

369

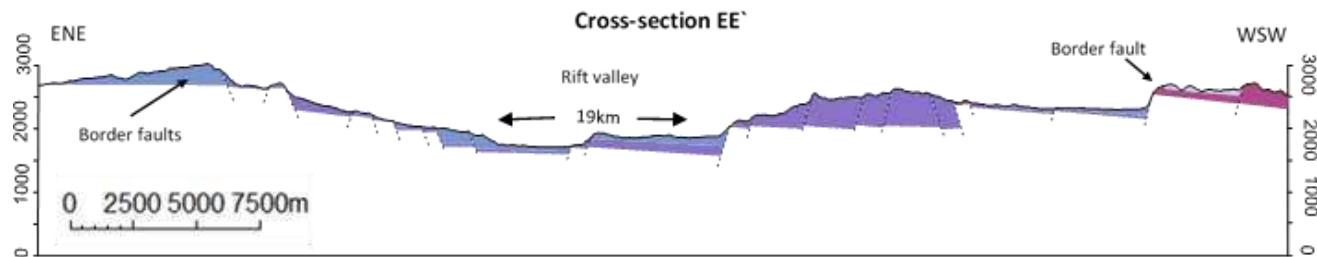


370

371

372

373



374

375

376

Figure 8. Cross-sections AA', BB' & CC' displaying the topographic profile, see Figure 1 Figure 7 for locations of these cross-section and the key of the geological units.

378

379

380

381

382

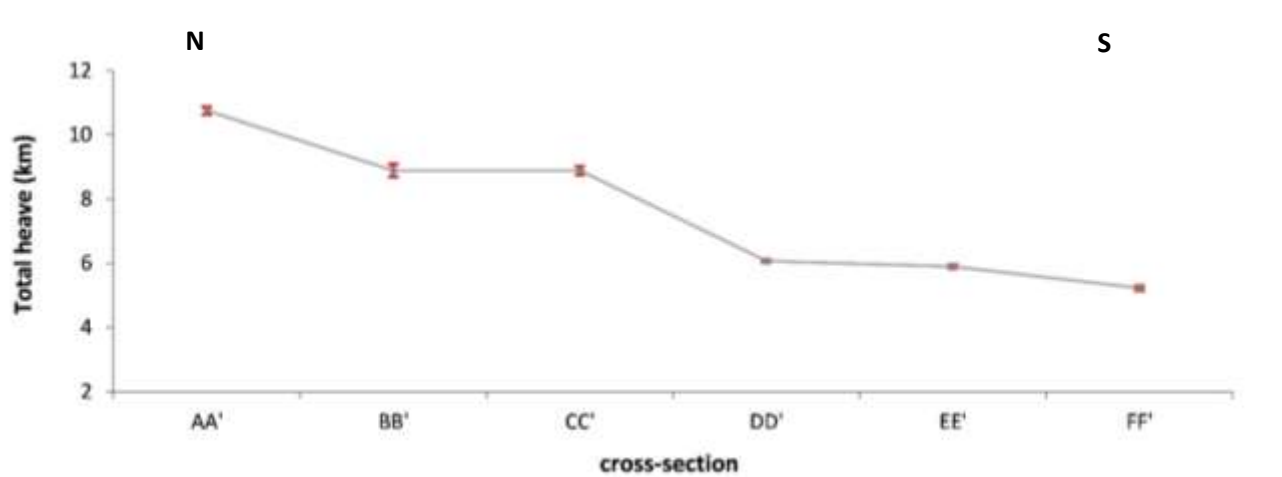
383

384

385 Table 1 Total fault heaves obtained from each cross-section (Figure 7)

386

Zones	Zone1		Zone2		Zone3	
Cross-sections	AA`	BB`	CC`	DD`	EE`	FF`
Total heaves measurement (m), (± uncertainty)	10748 (±126)	8884 (±199)	8882 (±133)	6066 (±45)	5896 (±63)	5226 (±77)
Average of total heave (m)	9816		7474		5561	
Heave percentage %	24	19	19	13	13	11
Length of cross-sections (Km)	107	92	78	44	83	70



405 Figure 9. Illustration showing the progressive increase of total heave (which is illustrative of strain, see section 4.3) from south to north. See Figure 7 for locations of cross-sections. Red bars represent calculated error in heave measurements.

406

407

408 4.4 Fault displacement populations

409 Table 2. Results of functions fit to displacement data

Rift zone	R ² for Function fits		
	Power-law	Log-normal	Exponential
zone 1	0.96	0.90	0.81
zone 2	0.93	0.91	0.82
zone 3	0.90	0.92	0.85
All zones	0.92	0.90	0.83

415 Fault displacement data for the three zones combined (Figure 10) and individually (Figure 11) were analysed
 416 using fault cumulative frequency log-log plots, and three statistical models including power law, log-normal
 417 and exponential laws were used to assess the best fit for the fault displacement populations. Generally power
 418 law scaling was found to be the best statistical model to fit the displacement data based upon the values of
 419 coefficient of determination R² (Table 2).

420 It has been shown in the literature that power law is preferred over other statistical distributions because it
 421 provides a better description of fault size distributions (e.g. Bonnet et al., 2001). For this reason, the power-
 422 law distribution is used in this study to assess the amount of deformation and to highlight the contribution
 423 of different fault sizes to the strain accommodation.

424 The exponents of the power-law distributions of fault displacement data from zone 1, zone 2 and zone 3
 425 were found to be 1.0, 1.1 & 1.4 respectively (Figure 11), and 1.2 for the three zones combined (Figure 10).
 426 These exponents are comparable to those obtained from a number of studies on tectonic fault systems that
 427 range from 1.0 to 1.5 (e.g. Scholz and Cowie, 1990, Marrett and Allmendinger, 1992, Gauthier and Lake,
 428 1993, Watterson et al., 1996, Yielding et al., 1996).

429 It is worth mentioning that large faults do not really follow the same trend as the mid-size faults (Figure 10
 430 & Figure 11), which might be because large faults accommodate disproportionately higher strain, leading to
 431 the steepening of population curves, as suggested by Bailey et al. (2005). Moreover, it can also be observed
 432 that there is an inverse correlation, where the lowest fractal dimension of $D = 1.0$ in zone 1 (Figure 10)
 433 corresponds to the largest average fault length and fault displacement of 7155 m and 660 m respectively
 434 (Table 3). On the other hand, the smallest average length and fault displacement of 5610 m and 450 m
 435 respectively corresponds to the highest fractal dimension of $D = \sim 1.4$ in zone 3; this issue is returned to
 436 later.

437 Table 3. Statistics of fault lengths and fault displacements in the three zones

438

439

	Length (m)			Displacement (m)		
	Min	Max	Average	Min	Max	Average
Zone 1 (n = 149)	1740	60600	7155	100	5160	660
Zone 2 (n = 295)	1270	54515	5775	40	6030	550
Zone 3 (n = 177)	1630	51477	5610	54	3939	450

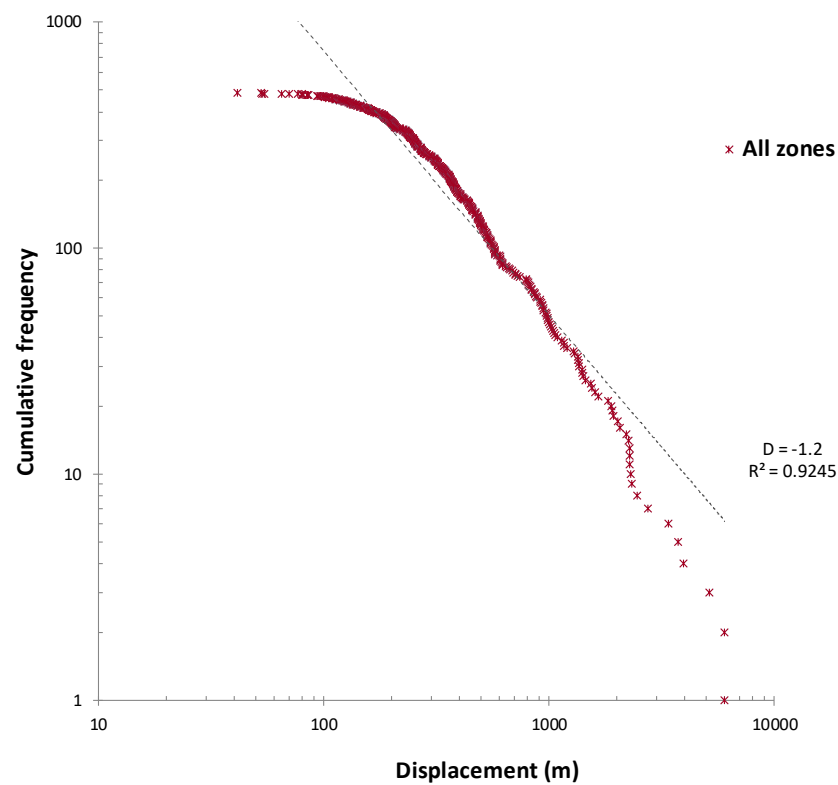


Figure 10. Displacement population showing a straight-line of power-law fitting with a slope of $D = -1.2$ in Log-Log plot for fault displacement against cumulative frequency for the three zones combined.

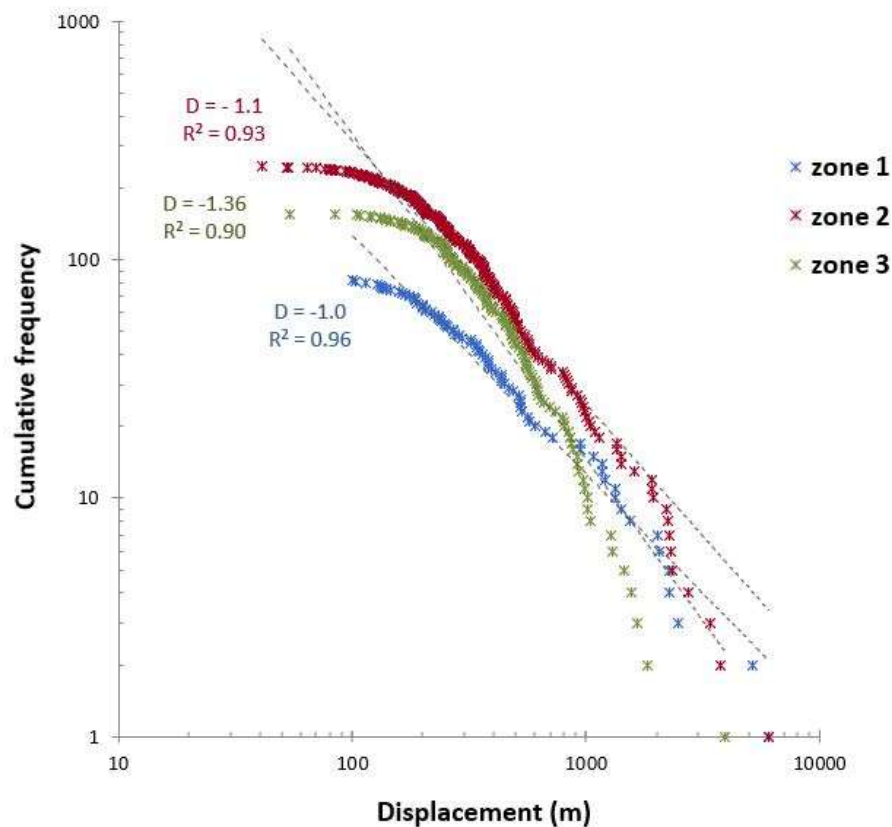


Figure 11. Log-Log plot for fault displacement against cumulative frequency for the three zones showing power-law function fit.

4.5 Fault length populations

Several studies have suggested that there is a strong correlation between fault displacement and fault length (e.g. Walsh and Watterson, 1988, Peacock and Sanderson, 1991, Cowie and Scholz, 1992a, Gillespie et al., 1993, Cartwright et al., 1995, Cowie, 1998b, Kim and Sanderson, 2005). Moreover, distribution of fault lengths should follow similar scaling relationships to fault displacement (Cladouhos and Marrett, 1996). Therefore, analysing attributes of fault length populations for the three zones using cumulative frequency function log-log plots would be expected to also show a power-law distribution. The power law exponent (D) for the length population for the three zones combined (Figure 12), and for each individual zone (Figure 13) was found to be ~ 1.4 , which is in agreement with the range of 1.0 to 1.7 from previously published fault length populations observed in natural fault systems (e.g. Gauthier and Lake, 1993, Scholz et al., 1993, Watterson et al., 1996). We notice here that the D values for the fault traces remain almost unchanged in the three zones; the implications of this will be discussed in the next section.

475

476

477

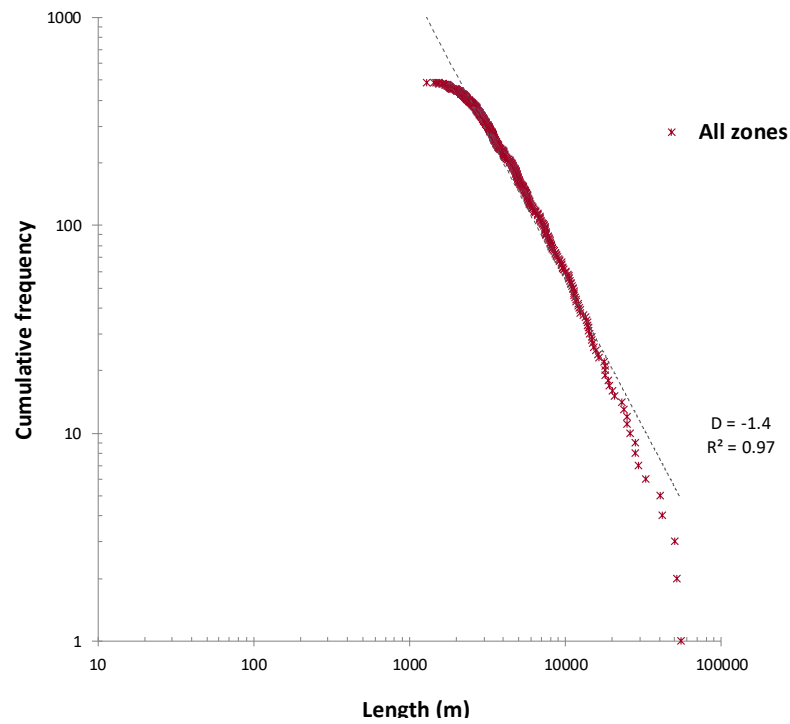


Figure 12. Log-Log plot of fault trace length vs cumulative frequency for all faults in the three zones.

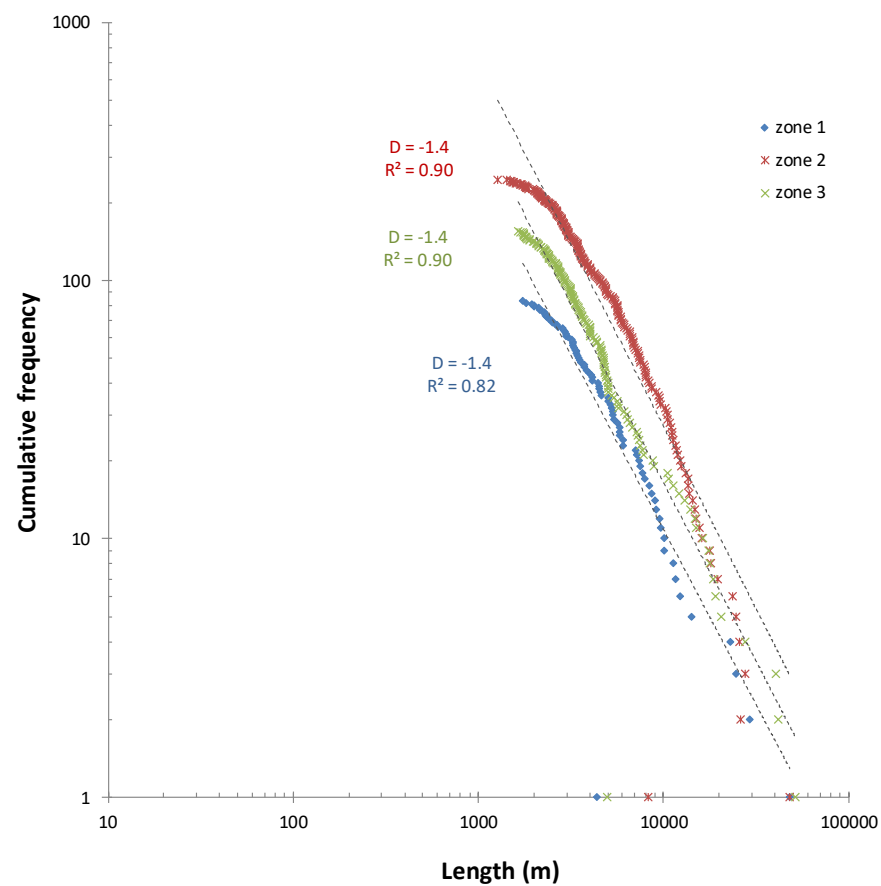


Figure 13. Log-Log plot of fault trace length vs cumulative frequency for the three zones showing power law fit.

478 **5 Discussion**

479 **5.1 Displacement-length scatter**

480 The datasets of 620 faults presented here is large enough to make reliable assessments and observations of
481 changes in geometry and behaviour of fault size attributes. which may shed light on the underlying physical
482 mechanism of fault growth and rift evolution. One possible limitation with the mapped faults in this study
483 is that the measured fault scarp height/ throw was not fully constrained. Accumulation of sedimentary and
484 volcanic deposits lower the apparent scarp height and would lead to underestimation of the displacement
485 values and, in turn, extension estimates and the D/L ratios. However, this has been overcome by the
486 application of a correction for the “hidden” throw. The displacement-length data for the mapped faults plot
487 generally within the field of displacement-length values compiled by Gillespie et al. (1992) and Bailey et al.
488 (2005) as shown in Figure 5. Therefore, we consider discussing results of this study in the light of published
489 literature of normal faults to be valid.

490 It has been observed from displacement-length data of each individual zone (Figure 6b, c, d) that several
491 faults have a comparable length but varying displacement. Such a vertical trend of increasing displacement
492 for given fault length will result in an increase of displacement-length ratio for larger faults (Walsh et al.,
493 2002a). Dawers et al. (1993) argued that the displacement-length relationship becomes non-linear in an
494 upward increasing manner when length is considered fixed relative to the cumulative slip from many slip
495 events. Therefore, the observed upward trend of increasing displacement population in each zone of the
496 study area (Figure 6 b, c, d) could be explained as follows: smaller faults that have experienced fewer slip
497 events should have lower displacement-length ratios than larger faults that have experienced more slip
498 events. This interpretation may be valid for the mapped faults in this study that occur in a single geological
499 setting, whilst recognising that previous research by Cowie and Scholz (1992a) suggests that the fault
500 displacement-length ratio may also be modified by material properties of the rock or if data are combined
501 from diverse geologic settings.

502 It has been mentioned in section 4 above that the scatter in any the maximum displacement-length data could
503 be caused by several sources; errors associated with the fault picks from the DEM surface could contribute
504 to the large scatter observed in this dataset (Figure 6). It also has been noted from the geological map of
505 Kenya (Figure 1) that the study area is covered by Quaternary and Tertiary volcanic sediments that could be
506 relatively uniform in lithology. Moreover, Smith (1994) indicated in his study that therefore, the lower
507 Miocene sediments deposited in central Kenya are predominantly volcanogenic. Therefore, it could be
508 argued that scattering shown by this dataset may be caused by other sources other than the rock lithology.
509 Another likely source that introduces scatter to plots of maximum displacement versus length of this dataset
510 is the process of fault growth through segment linkage, which is discussed further below.

511

512

513 **5.2 Strain distribution**

514 Extension regime in the central Kenya Rift is believed to occur in an approximately E-W direction, as
515 supported by geological data (Daly et al., 1989, Morley, 1988), current seismicity (Fairhead and Stuart,
516 1982, Foster and Jackson, 1998) and GPS analysis (Calais et al., 2006). The central Kenya Rift is thought
517 to be developed on a strongly heterogeneous basement, exhibiting a series of late Proterozoic, regional scale
518 NW-SE and NS trending ductile/brittle shear zones, which exist in the lithosphere beneath the rift (Daly et
519 al., 1989, Maurin and Guiraud, 1993, Mosley, 1993). Moreover, underlying basement fabric structures may
520 occur such as faults (Giba et al., 2012, Bellahsen and Daniel, 2005), shear zones (Corti, 2008, Agostini et
521 al., 2011, Corti, 2012) or foliations (Hetzl and Strecker, 1994) which could interfere with the regional stress
522 leading to localized variations in stress orientations (Aleksandrowski et al., 1992, Teyssier and Tikoff,
523 1999), and influence the orientation of normal faults during their initiation and evolution (Giba et al., 2012,
524 Bellahsen and Daniel, 2005, Agostini et al., 2009). Consequently, different orientations of fault populations
525 observed in the three zones (zone 1, 2 &3) in the central Kenya rift under the same regional extension
526 direction could be due to existence and influence of pre-existing structures with different orientations.

527 Estimation of strain through heave measurements along the study area (Figure 3.10a) exhibits that cross-
528 sections EE` and FF` in zone 3 in the south part of the rift also cross through a relatively large number of
529 faults but still have the least average heave percentage of ~12%, and that is because faults in zone 3 are
530 relatively smaller in size as indicated by the smallest average fault length and displacement (see Table 3).
531 Cross-sections CC` and DD` in zone 2 pass across a relatively larger number of faults and accommodate an
532 average heave percentage of ~16%. On the other hand, cross-sections AA` and BB in zone 1 in the north
533 accommodate the largest average heave percentage of ~22% along this part of the Rift. Table 3 displays that
534 zone 1 encompasses the fewest number of resolved faults (n = 149) and has the largest average of fault trace-
535 length and fault displacement. Therefore, differences in extensional strain accommodated between the
536 southern and northern zones of the study area are attributable to the extensional strain localization along a
537 few faults in the northern part (zone 1). These faults are deeper, with larger throws, and therefore take up
538 more extensional strain than those in the southern part (zone 3). These strain estimations suggest that zone
539 1 accommodates the largest amount of strain, followed by zone 2 then zone 3.

540

541 **5.3 Fault population analysis and implications for fault growth and rift evolution**

542 It has been demonstrated earlier that fault populations in the three defined zones (zone 1, zone 2 and zone
543 3), either individually or combined have exhibited a power-law distribution for both fault length and

544 displacement data. Fitting to a power law distribution for fault length populations in the three zones is
545 compatible with the low-strain settings of early continental Rifting (Gupta and Scholz, 2000, Vétel et al.,
546 2005). That contrasts with a high strain setting where rifts are more evolved and, therefore, an exponential
547 scaling function appears in the cumulative distribution for fault lengths as observed in the North Ethiopian
548 Rift–Afar transition area by Soliva and Schultz (2008), and in the Main Ethiopian Rift by Agostini et al.
549 (2011).

550 Differences in the exponent of power law scaling of fault size population distributions are used to assess the
551 contribution of different fault sizes to total strain accommodation (Yielding et al., 1996). The higher the
552 exponent of population slopes, D (fractal dimension), the higher the contribution of small faults to strain
553 accommodation (Marrett and Allmendinger, 1991, Yielding et al., 1996). This has been confirmed in the
554 current study for the examined fault displacement distributions (Figure 11), where zone 3 in the south
555 accommodates the least strain (Figure 9 & Table 1) and has the highest fractal dimension of $D = \sim 1.4$
556 (Figure 11). This implies that zone 3 encompasses a larger number of small faults contributing to the strain
557 accommodation compared to zone 2 and zone 1, and that is supported by the smallest averages of fault length
558 and fault displacement of 5610 m and 450 m respectively calculated for zone 3 (Table 3).

559 In the centre of the study area, the cumulative extension in zone 2 has increased to 7474m as opposed to
560 5561m in zone 3 (Figure 9 & Table 1). Consequently, the power law exponent of fault displacement
561 population decreases to $D = 1.1$ (Figure 11). Previous studies such as Cartwright et al. (1995) and Cladouhos
562 and Marrett (1996)) and experimental models e.g. Sornette et al. (1993) suggest that in all fault linkage
563 models, the fractal dimension (D value) of power-law distribution decreases systematically with increasing
564 fault strain as faults link. Thus, our observations suggest that zone 2 (where the averages of fault length and
565 displacement are greater than that of zone 3 as shown in Table 3) is a more mature fault zone with more
566 fault-linkage than zone 3.

567 Moreover, the fractal dimension for fault displacement decreases further to 1.0 in zone 1 (Figure 11) in the
568 north where the highest strain was estimated (Figure 9 & Table 1). It has been reported in some previous
569 studies (e.g. Cartwright et al., 1995, Cowie et al., 1995, Cladouhos and Marrett, 1996, Ackermann et al.,
570 2001, Walsh et al., 2003b, Moriya et al., 2005) that such a decrease of fractal dimension indicates that the
571 deformation is increasingly localised onto fewer large faults as the fault system. This has been supported in
572 this study by the greatest statistics of fault length and fault displacement calculated for zone 1 (Table 3)
573 where the fewest number of faults were mapped.

574 However, in many cases a simple power-law may not account for the full-range of the observed scaling
575 behaviour (Davy, 1993, Soliva and Schultz, 2008, Vétel et al., 2005). Among other factors that contribute

576 to the complexity of the fault network evolution, the boundary condition of the brittle layer may also affect
577 how the fault system evolves (Cowie et al., 2005, Hardacre and Cowie, 2003). Kudo and Furumoto (1998)
578 applied the fractal dimension analysis to characterize the crustal structures in three Japanese Islands, and
579 they observed changes in fractal dimension in the three areas, which were attributed to the lateral variation
580 of the crustal thickness in those areas. Therefore, it is worth mentioning that seismic refraction and regional
581 reflection studies of Henry et al. (1990a) and KRISP (1991) indicate significant variations in crustal
582 thickness between the craton and the mobile belt along the length of the Kenya Rift. Major crustal thinning
583 occurs along the axis of the Kenya Rift where the crustal thickness varies from 35 to 40 km in the south
584 beneath the central part of Kenya, within the vicinity of Lake Naivasha, to 18 -20 km in the north beneath
585 Lake Turkana. Therefore, the observed changes in fractal dimension of displacement distributions for the
586 three zones could also be due to variations in the crustal thickness of this region. However, the
587 abovementioned results may suggest more simply that rift zone 3 in the south is in a less mature stage than
588 rift zone 2 in the centre, and zone 2 is less developed than rift zone 1 in the northern part of the study area.
589 This phenomenon of northward increase in continental Rift evolution was also observed in the North
590 Ethiopian Rift–Afar transition area (Soliva and Schultz, 2008) and the Main Ethiopian Rifts (Agostini et al.,
591 2011). These inferences suggest that the processes of progressively increasing fault system maturity and
592 strain localization onto large faults could happen even over relatively small spatial scales (as small as this
593 study area, 240 x 150 km) within the same rift system.

594 In contrast to fractal dimensions of fault displacement populations (Figure 11) that decrease with increasing
595 strain, the power law distribution of fault length populations exhibit fractal dimensions of 1.4 (Figure 13), a
596 value which stays almost constant in the three zones despite increasing strain along the rift (Figure 9 &
597 Table 1). Previous studies of fault linkage suggest that fractal dimension decreases systematically with
598 increasing fault strain (e.g. Sornette et al., 1993, Cartwright et al., 1995, Cladouhos and Marrett, 1996). Such
599 stabilization of the fractal dimension of trace-length populations was interpreted by Poulimenos (2000) to
600 imply that linkage cessation is an important process for the evolution of the fault population over the
601 observed range of strains.

602 The observed relationship between the fractal dimension and strain for fault scaling properties is illustrated
603 in Figure 14, which may suggest that the fractal dimensions of fault population length is independent of
604 strain. In other words, the trace-length distribution is independent of strain and the increasing strain has no
605 effect on the fractal dimension of the fault length population.

606

607

608

609

610

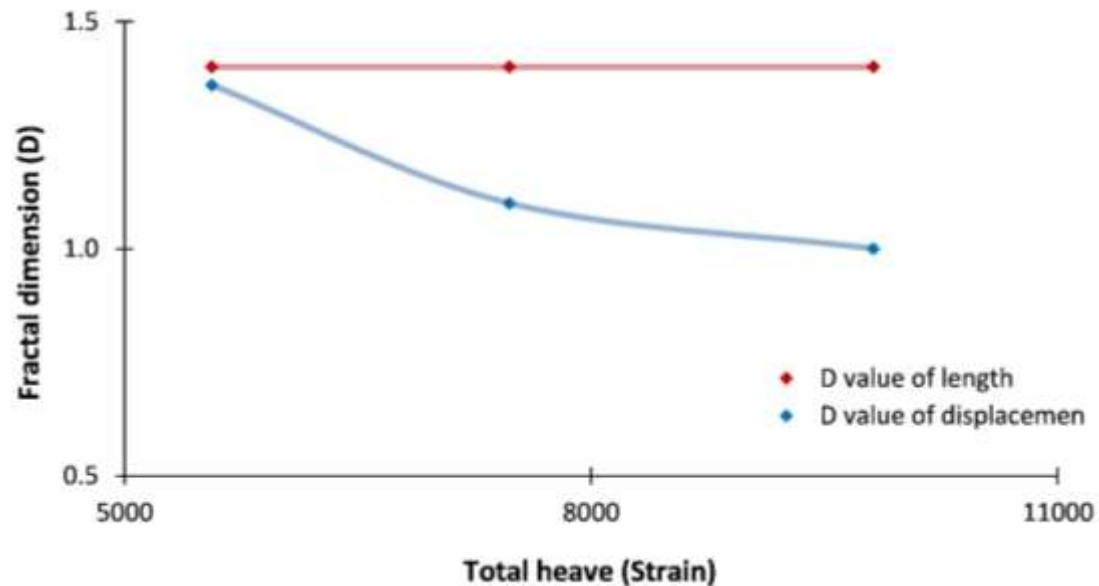
611

612

613

614

615



616

617

618

Figure 14. Illustration showing the observed relationship between the fractal dimension (D) and total heaves that represent strain for fault size attributes. Here, the D value of displacement population decreases with increasing strain, whereas the D value of length population remains almost constant as strain increases.

619

620

621

622

623

624

625

626

627

628

629

630

631

632

633

634

635

636

This would mean that with increasing strain, fault displacement increases, but fault lengths remain near constant. Moreover, these inferences support the observation of the vertical spread in the displacement population noticed in each zone of the study area (Figure 6 b, c, d). In this regard, this is consistent with the view that faults typically grow by steep or vertical growth trends rather than progressive increases both in displacement and in length (Walsh et al., 2002a, Nicol et al., 2010, Rotevatn et al., 2019). Similarly, vertical growth trends have also been observed in a natural normal fault system in the Timor Sea (Walsh et al., 2002a) and in analogue modelling (Schlagenhauf et al., 2008). Vertical growth trends like these require that, after initial rapid propagation, faults do not grow significantly in length (Walsh et al., 2002a, Nicol et al., 2010, Rotevatn et al., 2019). Therefore, these inferences are in line with the alternative/ coherent/ constant-length fault growth model suggested in previous studies (Walsh et al., 2002a, Walsh et al., 2003a, Childs et al., 2009, Giba et al., 2012, Jackson and Rotevatn, 2013, Rotevatn et al., 2019, Jackson et al., 2017, Nicol et al., 2016). This model has recently been referred to as the coherent constant-length model (Nicol et al., 2020). In that model, faults grow by rapidly establishing their near-maximum fault length in an early phase of deformation followed by accumulation of displacement with limited fault tip propagation. In this model, when strain fields of nearby isolated faults start to overlap and interact, as fault interactions are an essential feature of all fault systems (Walsh and Watterson, 1991), we see the instantaneous increase in fault length achieved by the coalescence and linkage of previously isolated faults (Walsh et al., 2002a, Rotevatn et al., 2019). The linked faults then begin to accrue displacement with no or little fault lengthening (Cartwright et

637 al., 1995). This process will result in the creation of large localized faults. It has been mentioned above that
638 the process of fault growth through segment linkage is an important factor to cause scatter in maximum
639 displacement-length data (e.g. Cartwright et al., 1995, Mansfield and Cartwright, 2001). Therefore,
640 segmented fault geometries could be responsible for the scatter in this dataset, which complicates the
641 establishment of any scaling law.

642 The rapid growth of fault length to near-maximum in the early stages of rifting has also been observed
643 further north in the Turkana Rift, north Kenya by Vétel et al. (2005) using fault displacement and length
644 data derived from outcrop studies, and digital elevation models. Moreover, the fault growth model is found
645 to be a dominant behaviour of normal fault growth in many extensional settings (e.g. Walsh et al., 2002a,
646 Walsh et al., 2003a, Giba et al., 2012). Therefore, the coherent constant-length model appears to be the most
647 plausible scenario for the mode of normal fault growth in the study area.

648 A study by Poulimenos (2000) in the active basin of the western Corinth Graben of central Greece, and
649 another study by Meyer et al. (2002) in the Vulcan Sub-basin of the Timor Sea, northwest Australia
650 examined fault growth of normal faults using fractal dimension analysis of fault size populations. Both
651 studies reached a similar conclusion to the current one, where fault lengths were established early during
652 extension of the basin and a later extension was largely accommodated by accumulation of displacements
653 with minimal fault propagation. However, those studies could not establish the generality of their findings
654 due to lack of detailed studies of the growth of fault populations with which their conclusions can be
655 compared. Thus, having compared the current study with those studies, it can be concluded that, in active
656 extensional setting, fractal dimension analysis appears to be a useful factor to describe the displacement-
657 length relationship in case the high scatter in displacement-length does not help in understanding the growth
658 of normal faults.

659

660

661

662

663

664

665

666 6 Conclusion

667 620 normal faults have been mapped from ASTER DEM surface data within the central Kenya Rift. Fault
668 trace lengths were corrected for resolution bias, and the extent of total fault throw into the subsurface was
669 estimated. The maximum displacement was therefore calculated using an average dip value for the study
670 area. Three fault populations have been identified within the study area according to their average fault strike
671 as zone 1 in the north, zone 2 in the centre & zone 3 in the south. The wide scale range of fault size
672 populations (maximum displacement of ~40 – ~6030 m; lengths of 1270 m to 60600 m) contained within
673 the data, allowed quantitative assessment of the scaling properties of the three fault populations, in order to
674 inform our understanding of the growth of normal faults. Estimations of extensional strain obtained from
675 six transects along the rift revealed a general increase of strain northward. Fault displacement data, analysed
676 by the cumulative frequency, obey a power-law distribution for the three zones of fault populations with
677 fractal dimension D of 1.0, 1.1 & 1.4 for zone 1, zone 2 and zone 3 respectively. Fault trace-length data also
678 conform to the same power-law relationships, but with D Values of ~1.4 for all three zones. Values of fractal
679 dimension of displacement distribution for the three zones showed a decrease with increasing strain as we
680 move from the south (zone3) through the centre (zone2) to the north (zone1) along the rift, which implies
681 that the strain is increasingly localised onto larger faults as the fault system evolves. In addition, values of
682 fractal dimension of fault length distributions remained almost unchanged in the three zones even with
683 increasing strain. Increasing fault displacement whilst the length remains almost fixed with increasing strain
684 along the study area may suggest that the fault system could be evolving in accordance to the coherent
685 constant-length fault growth model. Therefore, findings of this study suggest that the evolution of rift
686 deformation, can be observed even over relatively short spatial scales. It has also been concluded that
687 patterns of fault growth can be deduced from fractal dimension of cumulative distribution of fault size
688 populations.

689

690 **7 References**

- 691 ACKERMANN, R. V. & SCHLISCHE, R. W. 1997. Anticlustering of small normal faults around larger faults.
692 *Geology*, 25, 1127-1130.
- 693 ACKERMANN, R. V., SCHLISCHE, R. W. & WITHJACK, M. O. 2001. The geometric and statistical evolution of
694 normal fault systems: an experimental study of the effects of mechanical layer thickness on scaling
695 laws. *Journal of Structural Geology*, 23, 1803-1819.
- 696 AGOSTINI, A., BONINI, M., CORTI, G., SANI, F. & MAZZARINI, F. 2011. Fault architecture in the Main
697 Ethiopian Rift and comparison with experimental models: Implications for rift evolution and Nubia–
698 Somalia kinematics. *Earth and Planetary Science Letters*, 301, 479-492.
- 699 AGOSTINI, A., BONINI, M., CORTI, G., SANI, F. & MAZZARINI, F. 2011b. Fault architecture in the Main
700 Ethiopian Rift and comparison with experimental models: Implications for rift evolution and Nubia–
701 Somalia kinematics. *Earth and Planetary Science Letters*, 301, 479-492.
- 702 AGOSTINI, A., CORTI, G., ZEOLI, A. & MULUGETA, G. 2009. Evolution, pattern, and partitioning of
703 deformation during oblique continental rifting: Inferences from lithospheric-scale centrifuge
704 models. *Geochemistry, Geophysics, Geosystems*, 10, Q11015.
- 705 ALEKSANDROWSKI, P., INDERHAUG, O. H. & KNAPSTAD, B. 1992. Tectonic structures and wellbore
706 breakout orientation. *The 33th U.S. Symposium on Rock Mechanics (USRMS)*. Santa Fe, New
707 Mexico: American Rock Mechanics Association.
- 708 BAILEY, W. R., WALSH, J. J. & MANZOCCHI, T. 2005. Fault populations, strain distribution and basement
709 fault reactivation in the East Pennines Coalfield, UK. *Journal of Structural Geology*, 27, 913-928.
- 710 BAKER, B. H., MITCHELL, J. G. & WILLIAMS, L. A. J. 1988. Stratigraphy, geochronology and volcano-tectonic
711 evolution of the Kedong–Naivasha–Kinangop region, Gregory Rift Valley, Kenya. *Journal of the
712 Geological Society*, 145, 107-116.
- 713 BAKER, B. H., MOHR, P. A. & WILLIAMS, L. A. J. 1972. Geology of the Eastern Rift System of Africa. *Geological
714 Society of America Special Papers*, 136, 1-68.
- 715 BAKER, B. H. & WOHLBERG, J. 1971. Structure and Evolution of the Kenya Rift Valley. *Nature*, 229, 538-
716 542.
- 717 BELLAHSEN, N. & DANIEL, J. M. 2005. Fault reactivation control on normal fault growth: an experimental
718 study. *Journal of Structural Geology*, 27, 769-780.
- 719 BONNET, E., BOUR, O., ODLING, N. E., DAVY, P., MAIN, I., COWIE, P. & BERKOWITZ, B. 2001. Scaling of
720 fracture systems in geological media. *Reviews of Geophysics*, 39, 347-383.
- 721 CALAIS, E., EBINGER, C., HARTNADY, C. & NOCQUET, J. M. 2006. Kinematics of the East African Rift from
722 GPS and earthquake slip vector data. *Geological Society, London, Special Publications*, 259, 9-22.
- 723 CARTWRIGHT, J. A., MANSFIELD, C. & TRUDGILL, B. 1996. The growth of normal faults by segment linkage.
724 *Geological Society, London, Special Publications*, 99, 163-177.
- 725 CARTWRIGHT, J. A., TRUDGILL, B. D. & MANSFIELD, C. S. 1995. Fault growth by segment linkage: an
726 explanation for scatter in maximum displacement and trace length data from the Canyonlands
727 Grabens of SE Utah. *Journal of Structural Geology*, 17, 1319-1326.
- 728 CHILDS, C., MANZOCCHI, T., WALSH, J. J., BONSON, C. G., NICOL, A. & SCHÖPFER, M. P. J. 2009. A geometric
729 model of fault zone and fault rock thickness variations. *Journal of Structural Geology*, 31, 117-127.
- 730 CHOROWICZ, J. 2005. The East African rift system. *Journal of African Earth Sciences*, 43, 379-410.

- 731 CLADOUHOS, T. T. & MARRETT, R. 1996. Are fault growth and linkage models consistent with power-law
732 distributions of fault lengths? *Journal of Structural Geology*, 18, 281-293.
- 733 CORTI, G. 2008. Control of rift obliquity on the evolution and segmentation of the main Ethiopian rift.
734 *Nature Geoscience*, 1, 258-262.
- 735 CORTI, G. 2009. Continental rift evolution: From rift initiation to incipient break-up in the Main Ethiopian
736 Rift, East Africa. *Earth-Science Reviews*, 96, 1-53.
- 737 CORTI, G. 2012. Evolution and characteristics of continental rifting: Analog modeling-inspired view and
738 comparison with examples from the East African Rift System. Volumes 522–523, Pages 1–33.
- 739 COWIE, P. A. 1998a. Normal fault growth in three dimensions in continental and oceanic crust.
740 *GEOPHYSICAL MONOGRAPH-AMERICAN GEOPHYSICAL UNION*, 106, 325-348.
- 741 COWIE, P. A. 1998b. A healing–reloading feedback control on the growth rate of seismogenic faults. *Journal*
742 *of Structural Geology*, 20, 1075-1087.
- 743 COWIE, P. A. & SCHOLZ, C. H. 1992a. Displacement-length scaling relationship for faults: data synthesis and
744 discussion. *Journal of Structural Geology*, 14, 1149-1156.
- 745 COWIE, P. A. & SCHOLZ, C. H. 1992b. Growth of faults by accumulation of seismic slip. *Journal of*
746 *Geophysical Research: Solid Earth*, 97, 11085-11095.
- 747 COWIE, P. A., SORNETTE, D. & VANNESTE, C. 1995. Multifractal scaling properties of a growing fault
748 population. *Geophysical Journal International*, 122, 457-469.
- 749 COWIE, P. A., UNDERHILL, J. R., BEHN, M. D., LIN, J. & GILL, C. E. 2005. Spatio-temporal evolution of strain
750 accumulation derived from multi-scale observations of Late Jurassic rifting in the northern North
751 Sea: A critical test of models for lithospheric extension. *Earth and Planetary Science Letters*, 234,
752 401-419.
- 753 DALY, M. C., CHOROWICZ, J. & FAIRHEAD, J. D. 1989. Rift basin evolution in Africa: the influence of
754 reactivated steep basement shear zones. *Geological Society, London, Special Publications*, 44, 309-
755 334.
- 756 DAVIS, K., BURBANK, D. W., FISHER, D., WALLACE, S. & NOBES, D. 2005. Thrust-fault growth and segment
757 linkage in the active Ostler fault zone, New Zealand. *Journal of Structural Geology*, 27, 1528-1546.
- 758 DAVY, P. 1993. On the frequency-length distribution of the San Andreas fault system. *Journal of*
759 *Geophysical Research: Solid Earth*, 98, 12141-12151.
- 760 DAWERS, N. H., ANDERS, M. H. & SCHOLZ, C. H. 1993. Growth of normal faults: Displacement-length
761 scaling. *Geology*, 21, 1107-1110.
- 762 EBINGER, C. J. 1989. Tectonic development of the western branch of the East African rift system. *Geological*
763 *Society of America Bulletin*, 101, 885-903.
- 764 FAIRHEAD, J. D. & STUART, G. W. 1982. The Seismicity of the East African Rift System and Comparison with
765 Other Continental Rifts. *Continental and Oceanic Rifts*. American Geophysical Union.
- 766 FOSSEN, H. & HESTHAMMER, J. 1997. Geometric analysis and scaling relations of deformation bands in
767 porous sandstone. *Journal of Structural Geology*, 19, 1479-1493.
- 768 FOSTER, A. N. & JACKSON, J. A. 1998. Source parameters of large African earthquakes: implications for
769 crustal rheology and regional kinematics. *Geophysical Journal International*, 134, 422-448.
- 770 GAUTHIER, B. & LAKE, S. 1993. Probabilistic modeling of faults below the limit of seismic resolution in
771 Pelican Field, North Sea, offshore United Kingdom. *AAPG Bulletin*, 77, 761-777.

- 772 GIBA, M., WALSH, J. J. & NICOL, A. 2012. Segmentation and growth of an obliquely reactivated normal
773 fault. *Journal of Structural Geology*, 39, 253-267.
- 774 GILLESPIE, P. A., HOWARD, C. B., WALSH, J. J. & WATTERSON, J. 1993. Measurement and characterisation
775 of spatial distributions of fractures. *Tectonophysics*, 226, 113-141.
- 776 GILLESPIE, P. A., WALSH, J. J. & WATTERSON, J. 1992. Limitations of dimension and displacement data from
777 single faults and the consequences for data analysis and interpretation. *Journal of Structural*
778 *Geology*, 14, 1157-1172.
- 779 GILLESPIE, P. A., WALSH, J. J., WATTERSON, J., BONSON, C. G. & MANZOCCHI, T. 2001. Scaling relationships
780 of joint and vein arrays from The Burren, Co. Clare, Ireland. *Journal of Structural Geology*, 23, 183-
781 201.
- 782 GUPTA, A. & SCHOLZ, C. H. 2000. Brittle strain regime transition in the Afar depression: Implications for
783 fault growth and seafloor spreading. *Geology*, 28, 1087-1090.
- 784 HARDACRE, K. M. & COWIE, P. A. 2003. Controls on strain localization in a two-dimensional elastoplastic
785 layer: Insights into size-frequency scaling of extensional fault populations. 108.
- 786 HAUTOT, S., TARITS, P., WHALER, K., LE GALL, B., TIERCELIN, J.-J. & LE TURDU, C. 2000. Deep structure of
787 the Baringo Rift Basin (central Kenya) from three-dimensional magnetotelluric imaging:
788 Implications for rift evolution. *Journal of Geophysical Research: Solid Earth*, 105, 23493-23518.
- 789 HEFFER, K. & BEVAN, T. Scaling relationships in natural fractures: data, theory, and application. European
790 Petroleum Conference, 1990. Society of Petroleum Engineers.
- 791 HENRY, W. J., MECHIE, J., MAGUIRE, P., KHAN, M., PRODEHL, C., KELLER, G. & PATEL, J. 1990a. A seismic
792 investigation of the Kenya Rift Valley. *Geophysical Journal International*, 100, 107-130.
- 793 HENRY, W. J., MECHIE, J., MAGUIRE, P. K. H., KHAN, M. A., PRODEHL, C., KELLER, G. R. & PATEL, J. 1990b. A
794 Seismic Investigation of the Kenya Rift Valley. *Geophysical Journal International*, 100, 107-130.
- 795 HETZEL, R. & STRECKER, M. R. 1994. Late Mozambique Belt structures in western Kenya and their influence
796 on the evolution of the Cenozoic Kenya Rift. *Journal of Structural Geology*, 16, 189-201.
- 797 JACKSON, C. A.-L., BELL, R. E., ROTEVATN, A. & TVEDT, A. B. 2017. Techniques to determine the kinematics
798 of synsedimentary normal faults and implications for fault growth models. *Geological Society,*
799 *London, Special Publications*, 439, 187-217.
- 800 JACKSON, C. A.-L. & ROTEVATN, A. 2013. 3D seismic analysis of the structure and evolution of a salt-
801 influenced normal fault zone: a test of competing fault growth models. *Journal of Structural*
802 *Geology*, 54, 215-234.
- 803 JACKSON, P. & SANDERSON, D. J. 1992. Scaling of fault displacements from the Badajoz-Cordoba shear
804 zone, SW Spain. *Tectonophysics*, 210, 179-190.
- 805 JONES, W. B. & LIPPARD, S. J. 1979. New age determinations and the geology of the Kenya Rift-Kavirondo
806 Rift junction, W Kenya. *Journal of the Geological Society*, 136, 693-704.
- 807 KIM, Y.-S. & SANDERSON, D. J. 2005. The relationship between displacement and length of faults: a review.
808 *Earth-Science Reviews*, 68, 317-334.
- 809 KRISP, W. G. 1991. Large-scale variation in lithospheric structure along and across the Kenya rift *Nature*,
810 354.
- 811 KUDO, T. & FURUMOTO, M. 1998. Characterization of crustal structures by fractal analysis of gravity
812 anomalies. *Proceedings of the Japan Academy, Series B*, 74, 69-74.

- 813 LE GALL, B., NONNOTTE, P., ROLET, J., BENOIT, M., GUILLOU, H., MOUSSEAU-NONNOTTE, M., ALBARIC, J.
814 & DEVERCHÈRE, J. 2008. Rift propagation at craton margin.: Distribution of faulting and volcanism
815 in the North Tanzanian Divergence (East Africa) during Neogene times. *Tectonophysics*, 448, 1-19.
- 816 MANSFIELD, C. & CARTWRIGHT, J. 2001. Fault growth by linkage: observations and implications from
817 analogue models. *Journal of Structural Geology*, 23, 745-763.
- 818 MARIITA, N. O. & KELLER, G. R. 2007. An integrated geophysical study of the northern Kenya rift. *Journal*
819 *of African Earth Sciences*, 48, 80-94.
- 820 MARRETT, R. & ALLMENDINGER, R. W. 1991. Estimates of strain due to brittle faulting: sampling of fault
821 populations. *Journal of Structural Geology*, 13, 735-738.
- 822 MARRETT, R. & ALLMENDINGER, R. W. 1992. Amount of extension on "small" faults: An example from the
823 Viking graben. *Geology*, 20, 47-50.
- 824 MAURIN, J.-C. & GUIRAUD, R. 1993. Basement control in the development of the early cretaceous West
825 and Central African rift system. *Tectonophysics*, 228, 81-95.
- 826 MCCONNELL, R. B. 1972. Geological Development of the Rift System of Eastern Africa. *Geological Society*
827 *of America Bulletin*, 83, 2549-2572.
- 828 MEYER, V., NICOL, A., CHILDS, C., WALSH, J. & WATTERSON, J. 2002. Progressive localisation of strain during
829 the evolution of a normal fault population. *Journal of Structural Geology*, 24, 1215-1231.
- 830 MORIYA, S., CHILDS, C., MANZOCCHI, T. & WALSH, J. J. 2005. Analysis of the relationships between strain,
831 polarity and population slope for normal fault systems. *Journal of Structural Geology*, 27, 1113-
832 1127.
- 833 MORLEY, C. 1988. Variable extension in lake Tanganyika. *Tectonics*, 7, 785-801.
- 834 MORLEY, C. & NGENOH, D. 1999c. AAPG Studies in Geology# 44, Chapter 1: Introduction to the East African
835 Rift System.
- 836 MOSLEY, P. N. 1993. Geological evolution of the late Proterozoic "Mozambique Belt" of Kenya.
837 *Tectonophysics*, 221, 223-250.
- 838 NGENOH, D. K. A. 1993. Hydrocarbon potential of South Kerio Trough basin (Kenya) from seismic reflection
839 data. *M.Sc. thesis, University of Western Ontario: London, Canada 126 pp.*
- 840 NICOL, A., CHILDS, C., WALSH, J. J., MANZOCCHI, T. & SCHÖPFER, M. P. J. 2016. Interactions and growth of
841 faults in an outcrop-scale system. *Geological Society, London, Special Publications*, 439.
- 842 NICOL, A., WALSH, J., CHILDS, C. & MANZOCCHI, T. 2020. The growth of faults. *Understanding Faults*.
843 Elsevier.
- 844 NICOL, A., WALSH, J., VILLAMOR, P., SEEBECK, H. & BERRYMAN, K. 2010. Normal fault interactions,
845 paleoearthquakes and growth in an active rift. *Journal of Structural Geology*, 32, 1101-1113.
- 846 OMENDA, P. A. 2010. THE GEOLOGY AND GEOTHERMAL ACTIVITY OF THE EAST AFRICAN RIFT.
- 847 PEACOCK, D. 2002. Propagation, interaction and linkage in normal fault systems. *Earth-Science Reviews*,
848 58, 121-142.
- 849 PEACOCK, D. C. P. & SANDERSON, D. J. 1991. Displacements, segment linkage and relay ramps in normal
850 fault zones. *Journal of Structural Geology*, 13, 721-733.
- 851 PETIT, C. & EBINGER, C. 2000. Flexure and mechanical behavior of cratonic lithosphere: Gravity models of
852 the East African and Baikal rifts. *Journal of Geophysical Research: Solid Earth*, 105, 19151-19162.

- 853 PICKERING, G., BULL, J. M. & SANDERSON, D. J. 1995. Sampling power-law distributions. *Tectonophysics*,
854 248, 1-20.
- 855 PICKERING, G., PEACOCK, D. C. P. & LEE, J. M. 1997. Modeling Tip Zones to Predict the Throw and Length
856 Characteristics of Faults1. *AAPG Bulletin*, 81, 82-99.
- 857 POPE, D. A. 1992. Analyses and interpretations of the seismic reflection profiles from the Kerio Valley,
858 Kenya Rift. *M.Sc. thesis, University of Leeds (1992), p. 133.*
- 859 POULIMENOS, G. 2000. Scaling properties of normal fault populations in the western Corinth Graben,
860 Greece: implications for fault growth in large strain settings. *Journal of Structural Geology*, 22, 307-
861 322.
- 862 ROTEVATN, A., JACKSON, C. A. L., TVEDT, A. B. M., BELL, R. E. & BLÆKKAN, I. 2019. How do normal faults
863 grow? *Journal of Structural Geology*, 125, 174-184.
- 864 SCHLAGENHAUF, A., MANIGHETTI, I., MALAVIEILLE, J. & DOMINGUEZ, S. 2008. Incremental growth of
865 normal faults: Insights from a laser-equipped analog experiment. *Earth and Planetary Science*
866 *Letters*, 273, 299-311.
- 867 SCHLISCHE, R. W., YOUNG, S. S., ACKERMANN, R. V. & GUPTA, A. 1996. Geometry and scaling relations of
868 a population of very small rift-related normal faults. *Geology*, 24, 683-686.
- 869 SCHOLZ, C. H. & COWIE, P. A. 1990. Determination of total strain from faulting using slip measurements.
870 *Nature*, 346, 837-839.
- 871 SCHOLZ, C. H., DAWERS, N. H., YU, J. Z., ANDERS, M. H. & COWIE, P. A. 1993. Fault growth and fault scaling
872 laws: Preliminary results. *Journal of Geophysical Research: Solid Earth*, 98, 21951-21961.
- 873 SCHULTZ, R. A. & FOSSEN, H. 2002. Displacement–length scaling in three dimensions: the importance of
874 aspect ratio and application to deformation bands. *Journal of Structural Geology*, 24, 1389-1411.
- 875 SMITH, M. 1994. Stratigraphic and structural constraints on mechanisms of active rifting in the Gregory
876 Rift, Kenya. *Tectonophysics*, 236, 3-22.
- 877 SMITH, M. & MOSLEY, P. 1993. Crustal heterogeneity and basement influence on the development of the
878 Kenya Rift, East Africa. *Tectonics*, 12, 591-606.
- 879 SOLIVA, R., BENEDICTO, A. & MAERTEN, L. 2006. Spacing and linkage of confined normal faults: Importance
880 of mechanical thickness. *Journal of Geophysical Research: Solid Earth*, 111, n/a-n/a.
- 881 SOLIVA, R. & SCHULTZ, R. A. 2008. Distributed and localized faulting in extensional settings: Insight from
882 the North Ethiopian Rift–Afar transition area. *Tectonics*, 27, n/a-n/a.
- 883 SORNETTE, A., DAVY, P. & SORNETTE, D. 1993. Fault growth in brittle-ductile experiments and the
884 mechanics of continental collisions. *Journal of Geophysical Research: Solid Earth*, 98, 12111-12139.
- 885 STANTON-YONGE, A., CEMBRANO, J., GRIFFITH, W., JENSEN, E. & MITCHELL, T. 2020. Self-similar length-
886 displacement scaling achieved by scale-dependent growth processes: Evidence from the Atacama
887 Fault System. *Journal of Structural Geology*, 133, 103993.
- 888 TEYSSIER, C. & TIKOFF, B. 1999. Fabric stability in oblique convergence and divergence. *Journal of Structural*
889 *Geology*, 21, 969-974.
- 890 TORABI, A., ALAEI, B. & LIBAK, A. 2019. Normal fault 3D geometry and displacement revisited: Insights from
891 faults in the Norwegian Barents Sea. *Marine and Petroleum Geology*, 99, 135-155.
- 892 TORABI, A. & BERG, S. S. 2011. Scaling of fault attributes: A review. *Marine and Petroleum Geology*, 28,
893 1444-1460.

- 894 VÉTEL, W., LE GALL, B. & WALSH, J. J. 2005. Geometry and growth of an inner rift fault pattern: the Kino
895 Sogo Fault Belt, Turkana Rift (North Kenya). *Journal of Structural Geology*, 27, 2204-2222.
- 896 WALSH, J., NICOL, A. & CHILDS, C. A New Model for the Growth of Faults. 64th EAGE Conference &
897 Exhibition, 2002b.
- 898 WALSH, J., WATTERSON, J. & YIELDING, G. 1991. The importance of small-scale faulting in regional
899 extension. *Nature*, 351, 391-393.
- 900 WALSH, J. J., BAILEY, W. R., CHILDS, C., NICOL, A. & BONSON, C. G. 2003a. Formation of segmented normal
901 faults: a 3-D perspective. *Journal of Structural Geology*, 25, 1251-1262.
- 902 WALSH, J. J., CHILDS, C., IMBER, J., MANZOCCHI, T., WATTERSON, J. & NELL, P. A. R. 2003b. Strain
903 localisation and population changes during fault system growth within the Inner Moray Firth,
904 Northern North Sea. *Journal of Structural Geology*, 25, 307-315.
- 905 WALSH, J. J., NICOL, A. & CHILDS, C. 2002a. An alternative model for the growth of faults. *Journal of*
906 *Structural Geology*, 24, 1669-1675.
- 907 WALSH, J. J. & WATTERSON, J. 1988. Analysis of the relationship between displacements and dimensions
908 of faults. *Journal of Structural Geology*, 10, 239-247.
- 909 WALSH, J. J. & WATTERSON, J. 1991. Geometric and kinematic coherence and scale effects in normal fault
910 systems. *Geological Society, London, Special Publications*, 56, 193-203.
- 911 WALSH, J. J., WATTERSON, J., CHILDS, C. & NICOL, A. 1996. Ductile strain effects in the analysis of seismic
912 interpretations of normal fault systems. *Geological Society, London, Special Publications*, 99, 27-40.
- 913 WATTERSON, J. 1986. Fault dimensions, displacements and growth. *pure and applied geophysics*, 124, 365-
914 373.
- 915 WATTERSON, J., WALSH, J. J., GILLESPIE, P. A. & EASTON, S. 1996. Scaling systematics of fault sizes on a
916 large-scale range fault map. *Journal of Structural Geology*, 18, 199-214.
- 917 YIELDING, G., NEEDHAM, T. & JONES, H. 1996. Sampling of fault populations using sub-surface data: a
918 review. *Journal of Structural Geology*, 18, 135-146.
- 919 ZHANG, L. & EINSTEIN, H. H. 2000. Estimating the intensity of rock discontinuities. *International Journal of*
920 *Rock Mechanics and Mining Sciences*, 37, 819-837.
- 921 ZIEGLER, P. A. & CLOETINGH, S. 2004. Dynamic processes controlling evolution of rifted basins. *Earth-*
922 *Science Reviews*, 64, 1-50.
- 923 ZIELKE, O. & STRECKER, M. R. 2009. Recurrence of Large Earthquakes in Magmatic Continental Rifts:
924 Insights from a Paleoseismic Study along the Laikipia–Marmamet Fault, Subukia Valley, Kenya Rift.
925 *Bulletin of the Seismological Society of America*, 99, 61-70.
- 926